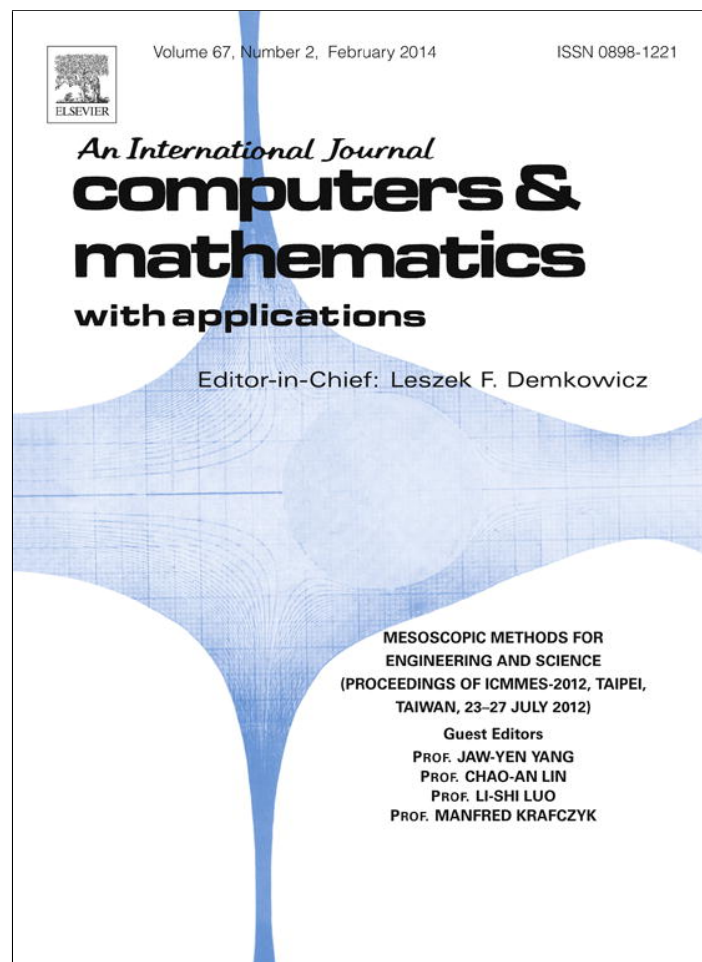


Provided for non-commercial research and education use.
Not for reproduction, distribution or commercial use.



This article appeared in a journal published by Elsevier. The attached copy is furnished to the author for internal non-commercial research and education use, including for instruction at the authors institution and sharing with colleagues.

Other uses, including reproduction and distribution, or selling or licensing copies, or posting to personal, institutional or third party websites are prohibited.

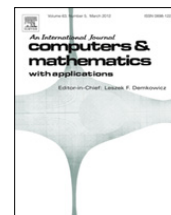
In most cases authors are permitted to post their version of the article (e.g. in Word or Tex form) to their personal website or institutional repository. Authors requiring further information regarding Elsevier's archiving and manuscript policies are encouraged to visit:

<http://www.elsevier.com/authorsrights>



Contents lists available at ScienceDirect

Computers and Mathematics with Applications

journal homepage: www.elsevier.com/locate/camwa

Study of forced turbulence and its modulation by finite-size solid particles using the lattice Boltzmann approach



Lian-Ping Wang^{a,b,*}, Orlando Ayala^{a,c}, Hui Gao^a, Charles Andersen^a, Kevin L. Mathews^a

^a Department of Mechanical Engineering, University of Delaware, Newark, DE 19716, USA

^b The State Key Laboratory of Coal Combustion, Huazhong University of Science and Technology, Wuhan, 430074, PR China

^c Department of Engineering Technology, Old Dominion University, Norfolk, VA 23529, USA

ARTICLE INFO

Keywords:

Particle-laden flow
Turbulence
Lattice Boltzmann equation
Finite-size effect
Particle–particle interactions
Particle-resolved simulation

ABSTRACT

The paper describes application of the mesoscopic lattice Boltzmann (LB) method to the simulations of both single-phase turbulence and particle-laden turbulence which are maintained by a large-scale forcing. The disturbance flows around finite-size solid particles are resolved, providing the opportunity to study the detailed interactions between fluid turbulence and solid particles at the particle–fluid interfaces. Specifically, a nonuniform time-dependent stochastic forcing scheme is implemented within the mesoscopic multiple-relaxation-time LB approach. The statistics of single-phase forced turbulence obtained from the LB approach are found to be in excellent agreement with those from the pseudo-spectral simulations, provided that the grid resolution in the LB simulation is doubled. It is shown that the flow statistics is not sensitive to the velocity scale used for the LB simulation. Preliminary results on forced turbulence laden with non-sedimenting solid particles at a particle-to-fluid density ratio of 5, solid volume fraction of 0.102, and particle diameter to Kolmogorov length ratio of 8.05 are interpreted, using a systematic analysis conducted at three levels: whole-field, phase-partitioned, and profiles as a function of distance from the surface of solid particles. It is found that the particle-laden turbulence is much more dissipative in terms of the non-dimensional dissipation rate, due to both reduction of the effective flow Reynolds number and the viscous boundary layer on the surfaces of solid particles. The thickness of the boundary layer is found to be about $0.4r_p$. While this boundary layer region accounts for 19.5% of the space within the fluid, it contributes to 57.5% of total viscous dissipation. The vorticity magnitude exhibits a maximum inside the boundary layer and a minimum outside the boundary layer, showing detachment of the vorticity structure from the solid surface. The sharp gradients near the particle surface contribute dominantly to the value of velocity derivative flatness, making the flatness in particle-laden flow much larger than that of single-phase turbulence. In the spectral space, presence of solid particles attenuates energy at large scales including the forcing shells and augments energy at the small scales. The pivot wavenumber is found to be very similar to the value previously found in decaying particle-laden turbulence under the similar parameter setting.

© 2013 Elsevier Ltd. All rights reserved.

* Corresponding author at: Department of Mechanical Engineering, University of Delaware, Newark, DE 19716, USA.
E-mail address: lwang@udel.edu (L.-P. Wang).

1. Introduction

Turbulent flows laden with solid particles, small droplets, and gas microbubbles are ubiquitous in engineering, biological and environmental applications. Examples include fluidized bed reactors, spray atomization, bubble columns, plankton contact dynamics in ocean water, transport of blood corpuscles in the human body, sediment transport, warm rain process, volcanic ash eruptions, dust storms, and sea sprays. In these applications, particles are usually suspended in a turbulent carrier fluid. The interactions between the dispersed and the carrier fluid phases impact the dynamics of suspended particles (e.g., dispersion, deposition rate, collision rate, and settling velocity) and the bulk properties of the multiphase flow (e.g., wall or surface drag, turbulence intensity and structures). Understanding turbulent particle-laden flows can help us better design engineering devices such as coal combustors and better predict natural phenomena such as warm rain and hurricane.

A turbulent particle-laden flow system is more complicated than its single-phase counterpart owing to a broader range of length and time scales and the additional parameters associated with the dispersed phase [1]. For a turbulent flow laden with non-deforming spherical particles, the length scales range from the particle diameter (d_p) and flow Kolmogorov length (η) to the integral length scale (L). When d_p/η is small and the volume fraction (ϕ) of the dispersed phase is low, the response of a particle to the local flow can be well described by an equation of motion [2], making it unnecessary to resolve the disturbance flow on the scale of the particle size. Most theoretical understanding for turbulent particle-laden flows has been developed based on these assumptions. Computationally, the condition of $d_p/\eta < 1$ partially justifies the use of point-particle based simulation (PPS) [3]. In the last 20 years, PPS has enabled researchers to discover and quantify a number of important phenomena in turbulent particle-laden flows including preferential concentration [4,5], turbulence modulation by inertial particles [6,7], particle deposition rate, and turbulent collision rate of inertial particles [3,8–11].

However, even for the relative simple case of small particle size, the interactions between the dispersed phase and the carrier phase are difficult to describe in general. For heavy particles whose density (ρ_p) is much larger than the fluid density (ρ_f), the ratio of the particle inertial response time (τ_p) to the flow Kolmogorov time (τ_k), known as the Stokes number, can be expressed as $St \equiv \tau_p/\tau_k = \frac{1}{18} (d_p/\eta)^2 (\rho_p/\rho_f)$, implying that particles could interact with a range of flow time scales depending on the relative magnitudes of the density and size ratios.

Many applications entail particle sizes comparable to or larger than the flow Kolmogorov length [12]. This introduces a finite-size effect greatly complicating the description of the multiphase flow system. Currently, the only rigorous method is to numerically resolve the disturbance flows around particles, known as the particle-resolved simulation (PRS). This requires an explicit implementation of the no-slip boundary condition on the surface of each particle, making PRS computationally more demanding than PPS. For this reason, PRS has so far been limited to either low flow Reynolds numbers or to large particle size relative to the Kolmogorov scale.

Several computational methods have been developed to perform PRS. These include finite element methods [13–15], the fictitious domain or direct forcing method [16–19], the immersed boundary method (IBM) [20–22], the force coupling method [23,24], the hybrid method Physalis [25–27], and the pseudo-penalization method [28]. These methods solve the continuum Navier–Stokes equation for the fluid flow, with different specific treatments at the fluid–solid interfaces.

In contrast, the mesoscopic lattice Boltzmann method (LBM) [29–31] realizes the flow field through local moments of a lattice Boltzmann equation using a uniform lattice grid. The no-slip boundary condition can be imposed by using a simple interpolated bounce-back scheme. To reduce force oscillations on the particles, the immersed-boundary–lattice–Boltzmann method (IB–LBM) [32,33] has also been developed by replacing the conventional bounce-back scheme with a direct forcing scheme applied on a set of Lagrangian boundary points representing particle surfaces.

Many of these particle-resolved simulation methods have been applied to study particle–particle interaction or particulate suspension in a non-turbulent fluid [34–37]. There have also been a few studies of particle-resolved simulation of turbulent particle-laden flows: in this case, the challenge is the multiscale nature involving a wide range of scales from the integral scale of the background turbulence to the scales of disturbance flows around each particle. For this reason, particle resolved simulation of turbulent particle-laden flows requires the state-of-the-art supercomputers. The dynamics of a single fixed or moving particle was simulated in [12,28,38,39]. Xu and Subramaniam [40] studied flow modulation by a group of fixed particles, and Tenneti et al. [41] examined drag forces on a random cluster of fixed spheres. Using a direct-forcing fictitious domain method, Wu et al. [18] and Shao et al. [19] investigated flow modulation by finite-size particles in the pipe and channel flows.

A limited number of studies on particle-laden turbulent flows using particle resolved simulations have also been reported [31,27,22,24,42], as reviewed in Gao et al. [43]. Using the lattice Boltzmann method, Gao et al. [43] studied modulation of decaying turbulence by solid particles under conditions similar to Lucci et al. [42]. They found that, at a given particle volume fraction, the dynamics of the particle-laden flow depended mainly on the effective particle surface area and particle Stokes number. The presence of finite-size inertial particles enhanced dissipation at small scales while reducing kinetic energy at large scales, with the normalized pivot wavenumber depending on the particle size, the ratio of particle size to flow scales, and particle-to-fluid density ratio. Using one-dimensional domain decomposition as the parallel implementation strategy, they were able to simulate a turbulent flow laden with $\mathcal{O}(100,000)$ particles.

The main goal of this paper is to extend the work of Gao et al. [43] to forced particle-laden turbulent flows. A forced stationary turbulence permits flow statistics to be averaged over time. The implementation of a large-scale forcing scheme within the lattice Boltzmann approach will be described in Section 2, along with a brief discussion on the parallel

implementation using two-dimensional and three-dimensional domain decompositions. In Section 3, we first validate the simulation of single-phase forced turbulence against pseudo-spectral simulation results, followed by a presentation of preliminary results on forced particle-laden flow. We will discuss whether the flow statistics are sensitive to the velocity scale setting in LBM. The results of particle-laden turbulence will be analyzed systematically at three levels: whole-field, phase partitioned, and profiles as a function of distance from the surface of a solid particle. Together, the results provide an in-depth understanding of the local interactions at the fluid–solid interfaces. Section 4 contains a summary and future outlook.

2. Simulation method

The particle-resolved simulation is based on the multiple-relaxation-time (MRT) lattice Boltzmann approach [44]. Since a thorough discussion of the method including a few validation cases has already been presented in [43], here we only summarize the essential components of the method. The applied large-scale forcing and scalable MPI implementation using multiple dimensional domain decompositions are new and will be described in detail in Sections 2.2 and 2.3.

2.1. The lattice Boltzmann (LB) approach

The MRT LB approach solves the evolution of mesoscopic particle distribution function by a lattice Boltzmann equation

$$\mathbf{f}(\mathbf{x} + \mathbf{e}_\alpha \delta t, t + \delta t) = \mathbf{f}(\mathbf{x}, t) - \mathbf{M}^{-1} \cdot \mathbf{S} \cdot [\mathbf{m} - \mathbf{m}^{(eq)}] + \mathbf{Q}, \quad (1)$$

where \mathbf{M} is an orthogonal transformation matrix converting the distribution function \mathbf{f} from discrete velocity space to the moment space \mathbf{m} , in which the collision relaxation is performed. The term \mathbf{Q} denotes a forcing field in the mesoscopic space to produce a desired non-uniform, time-dependent, large-scale physical space forcing field $\mathbf{F}(\mathbf{x}, t)$; its details will be discussed in Section 2.2. The transformation between the particle velocity space and the moment space is carried out by matrix operations as $\mathbf{m} = \mathbf{M} \cdot \mathbf{f}$, $\mathbf{f} = \mathbf{M}^{-1} \cdot \mathbf{m}$. The diagonal relaxation matrix \mathbf{S} specifies the relaxation rates for the non-conserved moments. The D3Q19 model was used and \mathbf{e}_α represents the discrete lattice velocities. Further details of the MRT LB approach can be found in [44]. The macroscopic hydrodynamic variables, including density ρ , momentum, and pressure p , are obtained from the moments of the mesoscopic distribution function \mathbf{f} , namely,

$$\rho = \rho_0 + \delta\rho, \quad \rho_0 = 1; \delta\rho = \sum_\alpha f_\alpha, \quad \rho_0 \mathbf{u} = \sum_\alpha f_\alpha \mathbf{e}_\alpha + \frac{\delta t}{2} \mathbf{F}(\mathbf{x}, t), \quad p = \delta\rho c_s^2 \quad (2)$$

where \mathbf{u} is the macroscopic fluid velocity, and the sound speed c_s is equal to $1/\sqrt{3}$ in lattice units. In our implementation, the above LB equation is only applied to the fluid lattice nodes.

An interpolated bounce-back scheme [45] was used to treat the interaction of the fluid with moving solid surfaces. When a particle moves, a solid lattice node may become a fluid node with unknown distribution functions. The missing distribution functions for the new fluid lattice node are constructed by an equilibrium distribution plus a non-equilibrium correction [46].

The hydrodynamic force \mathbf{F}_i acting on the i th particle is calculated during the interpolated bounce-back procedure by summing up the loss of fluid momentum on all the links across the surface of the i th particle, and the torque $\mathbf{\Gamma}_i$ acting on the i th particle is the sum of the cross product of the local position vector relative to the particle center and the loss of fluid momentum, over all boundary links. The particle translational velocity, position, angular velocity and displacement are then updated as

$$\mathbf{V}_i^{t+\delta t} = \mathbf{V}_i^t + \frac{1}{M_p} \left(\frac{\mathbf{F}_i^{t+\delta t/2} + \mathbf{F}_i^{t-\delta t/2}}{2} + \sum_j \mathbf{F}_{ij}^t \right) \delta t, \quad \mathbf{Y}_i^{t+\delta t} = \mathbf{Y}_i^t + \frac{1}{2} (\mathbf{V}_i^t + \mathbf{V}_i^{t+\delta t}) \delta t, \quad (3)$$

$$\mathbf{\Omega}_i^{t+\delta t} = \mathbf{\Omega}_i^t + \frac{1}{I_p} \left(\frac{\mathbf{\Gamma}_i^{t+\delta t/2} + \mathbf{\Gamma}_i^{t-\delta t/2}}{2} \right) \delta t, \quad \mathbf{\Theta}_i^{t+\delta t} = \mathbf{\Theta}_i^t + \frac{1}{2} (\mathbf{\Omega}_i^t + \mathbf{\Omega}_i^{t+\delta t}) \delta t \quad (4)$$

where M_p and $I_p \equiv \frac{2}{5} M_p R_i^2$ are the mass and moment of inertia of the i th particle, respectively, R_i is the particle radius, and \mathbf{F}_{ij} represents unresolved interaction force acting on the i th particle due to its interaction with j th particle (e.g., the lubrication force correction; see [47,48]). In this study, a simple pair-wise repulsive force model, same as what was used in [43], is applied to prevent particles from overlapping.

2.2. Implementation of large-scale forcing

We apply the well-known stochastic forcing scheme of Eswaran and Pope [49] to drive the turbulent flow. This forcing method has been used in numerous studies of single-phase and particle-laden turbulences (e.g., [5,50]) and has the advantage of predictable energy input. Using the same forcing scheme also allows us to compare our PRS results to PPS results such as the recent results of Abdelsamie and Lee [50]. The disadvantage of this scheme is that it requires a fast Fourier transform (FFT) to transform the large-scale forcing prescribed in the spectral space to the physical space. In this study,

we employ the recently developed highly-scalable FFT implementation using two-dimensional domain decomposition; see Ayala and Wang [51].

In the Eswaran–Pope forcing scheme an artificial forcing term is specified as a complex, vector-valued Uhlenbeck–Ornstein (UO) stochastic process. There are three parameters in the forcing scheme that determine the overall flow characteristics and energy input. The first is the forcing radius k_F , which determines how many modes are subjected to the forcing. In our study, 80 modes defined by $0 < |\mathbf{k}| < k_F = \sqrt{8}$ were forced. The other two parameters are the forcing amplitude σ_f and timescale T_f , which specify the standard deviation and the correlation time of the UO process, respectively. These together control the rate of energy addition (and thereby the dissipation rate) and the integral scales. In this work, we set $\sigma_f^2 = 447.3$ and $T_f = 0.038$, as in [5]. All values here are given in units of a pseudo-spectral simulation with a domain size of 2π . In the lattice Boltzmann simulation, the domain size is N lattice units, where N is the number of lattice cells in each spatial direction. The conversion between spectral units and lattice units will require a velocity scale V_s , representing the ratio of fluid velocity magnitude in lattice units to the velocity magnitude in spectral units. A basic requirement for nearly incompressible LB flow simulation is that the velocity magnitude in lattice units must be significantly smaller than the sound speed c_s , which will be met by choosing a proper V_s . We will study briefly how the simulated flow depends on the value of V_s .

According to the analysis of Eswaran and Pope [49], the average net rate of energy input through the forcing scheme, which is also equal to the average viscous dissipation rate, can be expressed empirically as

$$\text{rate of energy input} = \frac{4N_f \sigma_f^2 T_f}{1 + T_f (\sigma_f^2 T_f N_f k_0^2)^{1/3} / \beta}, \quad (5)$$

where the number of modes forced is $N_f = 80$ and the lowest wavenumber in spectral units is $k_0 = 1$. β is a fitting parameter. Based on their lower resolution simulations, Eswaran and Pope [49] found that $\beta \approx 0.8$. Using this β value, the rate of energy input is estimated to be 3564 in spectral units.

The first step in the forcing implementation is to generate a complex UO process for each mode in the spectral space with $0 < |\mathbf{k}| < \sqrt{8}$. When the minimum widths of all subdomains in the y and z directions are 6 and 3, respectively, only two processors are involved in setting up the UO processes for the forced modes in the spectral space. The vector field is then transformed to the physical space to produce $\mathbf{F}(\mathbf{x}, t)$. The mesoscopic forcing field, consistent with the incompressible MRT formulation and free from low-order discrete lattice errors, is given as [52,53]

$$\mathbf{Q} = \mathbf{M}^{-1} \left(\mathbf{I} - \frac{\mathbf{S}}{2} \right) \mathbf{M} \Phi \delta t, \quad \text{where } \Phi_\alpha = \rho_0 W_\alpha \left[\frac{\mathbf{e}_\alpha \cdot \mathbf{F}}{c_s^2} + \frac{\mathbf{uF} : (\mathbf{e}_\alpha \mathbf{e}_\alpha - c_s^2 \mathbf{I})}{c_s^4} \right]. \quad (6)$$

To reduce the number of matrix multiplications, we implemented the forcing scheme by introducing an intermediate variable, $\bar{\mathbf{f}}(\mathbf{x}, t) = \mathbf{f}(\mathbf{x}, t) + \Phi \delta t / 2$. Then Eqs. (1) and (6) can be combined to yield a compact form as

$$\mathbf{f}(\mathbf{x} + \mathbf{e}_\alpha \delta t, t + \delta t) = \bar{\mathbf{f}}(\mathbf{x}, t) - \mathbf{M}^{-1} \cdot \mathbf{S} \cdot [\mathbf{M} \bar{\mathbf{f}}(\mathbf{x}, t) - \mathbf{m}^{(\text{eq})}] + \Phi \frac{\delta t}{2}. \quad (7)$$

The forcing is applied at the collision step. We will validate this implementation of time-dependent non-uniform forcing by comparing, in Section 3.1, the simulated single-phase forced turbulence with results from a pseudo-spectral simulation. This comparison is a necessary step before preliminary results on forced particle-laden turbulent flow are presented. This comparison can also be viewed as an extension to the study of Peng et al. [54] on comparing LB and spectral simulations for decaying homogeneous isotropic turbulence. To our knowledge, such a direct comparison between LB and pseudo-spectral for a forced turbulence has not been attempted previously, although several papers reported simulations of forced turbulence by the LB approach [55–57]. In particular, we note that the simple forcing implementations used in [55,57] contain low-order discrete lattice errors according to Guo et al. [52]. We also note that these previous LB simulations of forced turbulence were done with the single-time relaxation (BGK) collision operator.

2.3. MPI implementation and scalability

In our previous implementation reported in Gao et al. [43], the code was parallelized using 1D domain decomposition. We have now implemented 2D and 3D domain decompositions to allow the use of a much larger number of processors. The basic idea is to divide the data and tasks according to the subdomains, namely, each processor handles the computational load within a subdomain. In addition to the implementation details reported in Gao et al. [43], we streamlined the data communication needs near the subdomain boundaries into two general categories. The first and the most common category is the forward data communication where some data from a current subdomain are sent to neighboring subdomains to provide information in the extended (or halo) zones of each subdomain. Examples include gathering of node/link information for processing boundary links, interpolating variables at off-grid locations from grid data, and constructing unknown distributions for new fluid lattice nodes. This is done in each of the decomposed direction sequentially. Data communication in each subsequent coordinate direction makes use of the updated subdomain data in coordinate directions that have already been communicated. In this manner, only two send–receive steps are needed in each coordinate direction and the data in the subdomain corners are automatically covered.

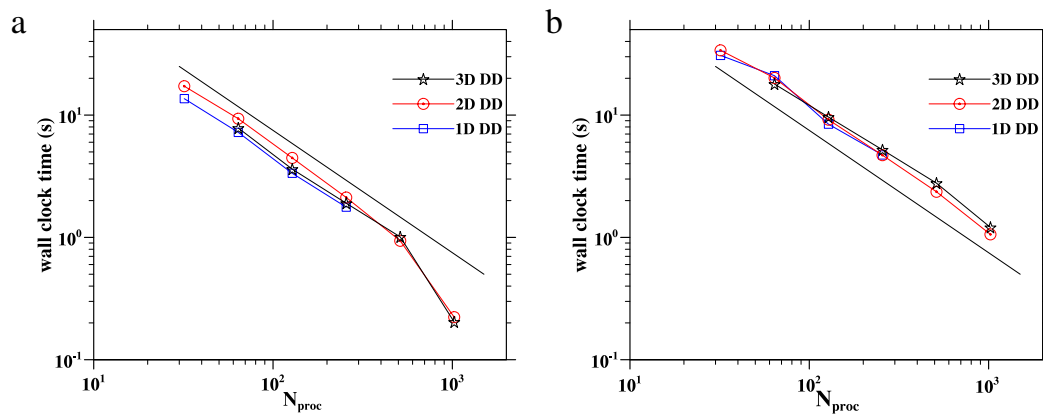


Fig. 1. Wall clock time as a function of the number of processors used: (a) single-phase turbulence simulation on 512^3 grid; (b) particle-laden flow on 512^3 grid and with 50,000 particles of diameter equal to 8 lattice units. Three domain decomposition strategies are compared.

The second category is the reverse data communication where some updated data in the neighboring subdomains must be collected by a current processor. A typical example is the redistribution of particles after their centers have been moved to a different subdomain. In this case, we first separate particles whose centers have been moved out of the current subdomain and re-pack the remaining particles with centers located within the current subdomain. All particles in the neighboring subdomains whose locations have been changed to the current subdomain are then identified and added to the current processor. Again data communications are done sequentially, one direction after another. The communication of data from corners is handled essentially in reverse when compared to the forward communication. In the end, each processor will contain all information of particles with centers located within the corresponding subdomain, with a reasonable load balancing.

Fig. 1 shows the scalability of the code for both single-phase turbulence simulations at 512^3 resolution and particle-laden flow simulations at 512^3 resolution with 50,000 solid particles of diameter equal to 8 lattice units. In general, the performance is similar for the different domain decompositions. When running the flow simulation with 1024 processors, the wall clock time is significantly less than what would be expected from the ideal scaling. This apparent super-scaling is a result of decreasing data size to the point that the fast cache memory becomes adequate in handling the data. The particle-laden flow code shows essentially ideal scaling up to 1024 processors tested. For particle-laden flows, the super-scaling was not observed for three reasons. First, the particle-laden flow code made use of quite a few global arrays for code simplicity [43], which increases the memory usage for each processor. Second, there is relatively more latency time associated with more data communication steps, when compared to the single-phase flow. Third, currently, the boundary link information is saved in 4D arrays for code simplicity, which is also memory intensive. We believe that this last aspect can be improved by using 1D, indexed arrays, so the memory requirement for treating boundary links can be drastically reduced.

3. Results

In this section, we present results on both single-phase and particle-laden turbulent flows driven by the large-scale stochastic forcing.

3.1. Single-phase forced turbulence

For the single-phase turbulence, the focus is on the comparison of the simulated flow statistics with results from pseudo-spectral simulation. We consider a setting that would lead to a well-resolved forced turbulence when the pseudo-spectral method is used at a grid resolution of 128^3 . The spectral resolution is typically measured by $k_{\max}\eta$, where $k_{\max} = \frac{1}{2}N - 1.5$ is the maximum wavenumber considered in the pseudo-spectral simulation and η is the Kolmogorov length. This resolution parameter is $k_{\max}\eta = 1.39$, and the resulting Taylor microscale flow Reynolds number is $R_\lambda = 74.3$. Four LB simulations were designed to match the same physical parameters as the pseudo-spectral simulation (see Table 1), with varying grid resolutions and velocity scale V_s , where V_s represents the ratio of velocity magnitude in the LB simulation to that in the pseudo-spectral simulation.

In Fig. 2 we plot the time evolution of volume-averaged flow kinetic energy and dissipation rate. The results from the LB simulations are converted back to the spectral units to allow for a direct comparison. The flow is initially at rest, and the large-scale forcing injects energy into the large scales, which is transferred to smaller scales. Eventually, the viscous dissipation balances the energy input from the large-scale forcing, and the flow becomes statistically stationary. Typically, it takes about 3–5 large-eddy turnover times for the flow to reach the stationary stage. The results from all simulations overlap initially, and their general features are very similar during the stationary stage.

Table 1

Parameter settings and simulated statistics in forced single-phase turbulent flows. The values in the lattice Boltzmann simulations have been transformed to the units in the pseudo-spectral simulation, except $|\mathbf{u}|_{\max}$. Note that the CFL number is defined as $(|u_1| + |u_2| + |u_3|)_{\max} dt/dx$ in the spectral code, while it is defined as $|\mathbf{u}|_{\max} dt/dx$ in the LBM code.

| Run | PS128 | LB128 | LB256H | LB256HR | LB512H2 |
|----------------------------------|----------------------|-----------------------|-----------------------|-----------------------|-----------------------|
| Grid resolution N^3 | 128^3 | 128^3 | 256^3 | 256^3 | 512^3 |
| Viscosity ν | 0.0945 | 0.0945 | 0.0945 | 0.0945 | 0.0945 |
| Time step dt | 1×10^{-4} | 1×10^{-4} | 0.5×10^{-4} | 0.25×10^{-4} | 0.2×10^{-4} |
| $V_s = Ndt/(2\pi)$ | – | 2.04×10^{-3} | 2.04×10^{-3} | 1.02×10^{-3} | 1.63×10^{-3} |
| ϵ per unit mass | 3475 ± 54 | 3549 ± 45 | 3570 ± 69 | 3581 ± 62 | 3648 ± 115 |
| u' | 18.63 ± 0.10 | 18.90 ± 0.09 | 18.70 ± 0.13 | 18.78 ± 0.11 | 18.83 ± 0.24 |
| R_λ | 74.3 ± 0.5 | 75.7 ± 0.5 | 74.0 ± 0.6 | 74.5 ± 0.6 | 74.2 ± 1.1 |
| $k_{\max}\eta$ | 1.39 | 1.38 | 2.79 | 2.79 | 5.60 |
| CFL | 0.289 | 0.24 | 0.25 | 0.13 | 0.18 |
| $ \mathbf{u} _{\max}$ (LB units) | – | 0.24 | 0.25 | 0.13 | 0.18 |
| Skewness S | -0.505 ± 0.001 | -0.450 ± 0.003 | -0.499 ± 0.003 | -0.487 ± 0.003 | -0.504 ± 0.004 |
| Flatness F | 4.794 ± 0.014 | 4.534 ± 0.014 | 4.859 ± 0.017 | 4.816 ± 0.020 | 4.872 ± 0.027 |
| η | 0.0222 ± 0.0001 | 0.0221 ± 0.0001 | 0.0221 ± 0.0001 | 0.0221 ± 0.0001 | 0.0220 ± 0.0002 |
| λ | 0.377 ± 0.002 | 0.379 ± 0.002 | 0.374 ± 0.002 | 0.375 ± 0.002 | 0.372 ± 0.003 |
| L_f | 1.07 ± 0.01 | 1.06 ± 0.01 | 1.05 ± 0.01 | 1.06 ± 0.01 | 1.049 ± 0.015 |
| τ_K | $(5.24 \pm 0.04)e-3$ | $(5.18 \pm 0.03)e-3$ | $(5.18 \pm 0.05)e-3$ | $(5.16 \pm 0.04)e-3$ | $(5.12 \pm 0.08)e-3$ |
| T_e | 0.1004 ± 0.0010 | 0.1013 ± 0.0010 | 0.0990 ± 0.0011 | 0.0993 ± 0.0011 | 0.0979 ± 0.0016 |
| $\Delta T_{\text{ave}}/T_e$ | 70.0 | 69.1 | 70.7 | 70.5 | 27.6 |
| $\epsilon L_f/(u')^3$ | 0.577 ± 0.023 | 0.556 ± 0.019 | 0.575 ± 0.028 | 0.570 ± 0.025 | 0.573 ± 0.048 |

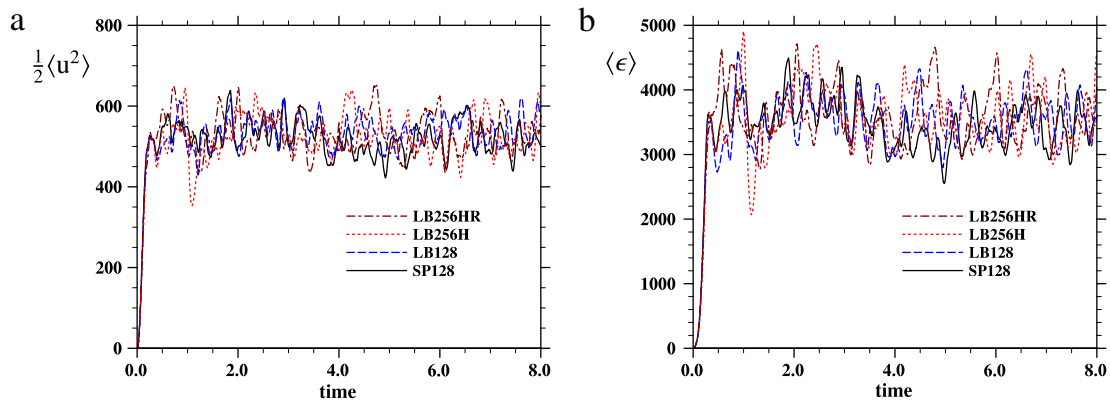


Fig. 2. Time evolution of (a) kinetic energy and (b) dissipation rate in the forced single-phase flow.

Each simulation except Run LB512H2 is run for about 80 eddy turnover times, and the volume-averaged statistics are further averaged over the last 70 eddy turnover times. The resulting statistics are shown in Table 1. The opportunity to average over 70 eddy turnover times provides a way to estimate the standard deviation of the final averaged value. Let σ_A be the standard deviation of volume-averaged quantity $A(t)$. The standard deviation of the time-averaged A , namely, $\bar{\sigma}_A \equiv \frac{1}{\Delta T_{\text{ave}}} \int_{t_0}^{t_0 + \Delta T_{\text{ave}}} A(t) dt$, is [49]

$$\bar{\sigma}_A = \sigma_A \sqrt{\frac{2T_c}{\Delta T_{\text{ave}}}}, \tag{8}$$

where T_c is the correlation time of $A(t)$, and ΔT_{ave} is the time duration used for averaging. We computed the correlation coefficient, $R(\tau) \equiv \langle A(t_1)A(t_1 + \tau) \rangle / \sigma_A^2$, and T_c is estimated by simply setting $R(T_c) = 0.5$. In Table 1, we list the statistics in the form of $\bar{A} \pm \bar{\sigma}_A$.

In addition to the three forcing parameters (N_f , σ_f^2 , and T_f) and V_s (for LB flow simulation), the flow-simulation input parameters are: the grid resolution N , kinematic viscosity ν , and the time step dt . The computed flow statistics at the stationary stage, listed in Table 1, include the flow dissipation rate ϵ , r.m.s. component fluctuation velocity u' , Taylor microscale flow Reynolds number R_λ , resolution parameter $k_{\max}\eta$, CFL number, the maximum velocity magnitude $|\mathbf{u}|_{\max}$ in LB units, velocity derivative skewness S , velocity derivative flatness, Kolmogorov length η , transverse Taylor microscale $\lambda = \sqrt{15\nu u'^2/\epsilon}$, longitudinal integral length scale L_f , Kolmogorov time τ_K , eddy turnover time $T_e = u'^2/\epsilon$, the normalized averaging time interval $\Delta T_{\text{ave}}/T_e$, and the normalized dissipation rate $\epsilon L_f/(u')^3$.

As noted previously, according to Eswaran and Pope [49], the expected flow dissipation rate is around 3564. This value is consistent to what are realized in the simulations, considering the levels of statistical uncertainty as indicated by the standard deviations. The low-resolution LB simulation, LB128, yields a slightly larger u' , smaller magnitudes of velocity

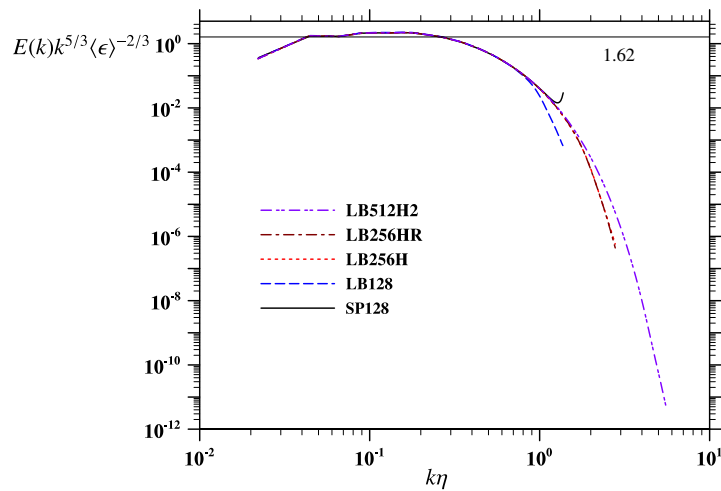


Fig. 3. Compensated kinetic energy spectra of forced single-phase flow. The horizontal line shows the expected level in the inertial subrange.

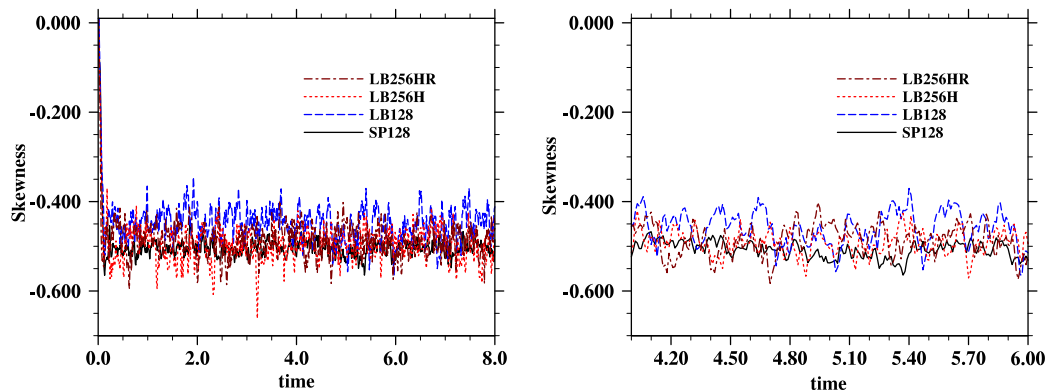


Fig. 4. Time evolution of velocity-derivative skewness. The right panel is a zoom-in view of a portion of what is shown in the left panel.

derivative skewness and flatness, and smaller normalized dissipation rate, when compared to the benchmark values from the pseudo-spectral simulation. Other three higher resolution LB simulations produce matching values of statistics when compared to those from the pseudo-spectral simulation (the only exception is perhaps the velocity derivative skewness, which will be discussed below). In particular, they all yield a normalized flow dissipation of $\epsilon L_f / (u')^3 \approx 0.575 \pm 0.025$. The general conclusion is that the LB simulation, due to its overall second-order spatial accuracy, would require twice the grid resolution to produce similar statistics as the pseudo-spectral simulation, in agreement with the conclusion of Peng et al. [54] who compared LB simulation and pseudo-spectral simulation for decaying turbulence. The different values of velocity scale V_s appear to have a negligible effect of the overall flow statistics.

Fig. 3 provides a comparison of compensated energy spectra from various simulations. Since the pseudo-spectral simulation is not fully de-aliased, a minor upward tail is present near the maximum $k\eta$. Except the run LB128, all LB runs provide the same spectrum as the pseudo-spectral simulation. This again confirms that twice of the spatial resolution is needed for the LB simulation to reproduce the spectral accuracy. Note that the two runs LB256H and LB256HR yield an identical spectrum. The best benchmark of the spectrum in the high wavenumber region should be that from LB512H2. Increasing resolution in LB simulations leads to better representation of the spectrum in the far-dissipation region ($k\eta > 1$).

We also compare the time evolutions of skewness and flatness in Figs. 4 and 5, respectively. Careful examination of Fig. 4 reveals two differences of LB results from the pseudo-spectral simulation. First, there appears to be large fluctuations in the skewness from the LB simulation. Second, the skewness in the LB simulation is slightly less in magnitude for most of the time, when compared with the pseudo-spectral result. However, occasional spikes of large magnitudes in skewness are also evident. Similar features in the LB velocity derivative flatness are also observed in Fig. 5. The spikes and large fluctuations are related to acoustic waves inherent in the LB method, as pointed out in Peng et al. [54]. These spikes could be further amplified by the bounce-back scheme on the solid surface in the particle-laden flows. It may be possible to reduce the fluctuations in MRT-LB by optimizing the relaxation parameters. A close inspection of Figs. 4 and 5 indeed indicates that the non-physical part of the fluctuations is smaller in LB256HR when compared to those in LB256H. A systematic study of tuning all relaxation parameters is beyond the scope of the current study. This aspect, although having little impact on the overall flow statistics, deserves further investigation.

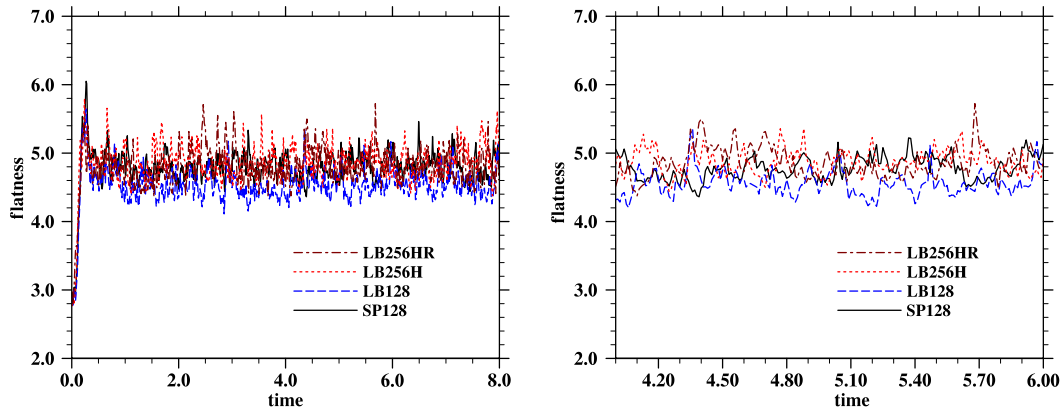


Fig. 5. Time evolution of velocity-derivative flatness. The right panel is a zoom-in view of a portion of what is shown in the left panel.

Table 2

Parameter settings and simulated statistics in forced particle-laden turbulent flows. The values in the lattice Boltzmann simulations have been transformed to the units in the pseudo-spectral simulation, except $|\mathbf{u}|_{\max}$ and $|\mathbf{v}|_{\max}$.

| Run | LB256HP | LB256HRP | LB5 12H2P |
|----------------------------------|-----------------------|-----------------------|-----------------------|
| Grid resolution N^3 | 256^3 | 256^3 | 512^3 |
| Viscosity ν | 0.0945 | 0.0945 | 0.0945 |
| Time step dt | 0.5×10^{-4} | 0.25×10^{-4} | 0.20×10^{-4} |
| $V_s = Ndt / (2\pi)$ | 2.04×10^{-3} | 1.02×10^{-3} | 1.63×10^{-3} |
| ϵ^{full} per unit mass | 2414 ± 63 | 2424 ± 73 | 2532 ± 123 |
| u' | 13.16 ± 0.13 | 13.15 ± 0.15 | 13.46 ± 0.19 |
| R_λ | 44.6 ± 0.3 | 44.5 ± 0.4 | 45.5 ± 0.8 |
| $k_{\max} \eta$ | 3.08 | 3.08 | 6.13 |
| $ \mathbf{u} _{\max}$ (LB units) | 0.17 | 0.088 | 0.135 |
| $ \mathbf{v} _{\max}$ (LB units) | 0.13 | 0.069 | 0.092 |
| Skewness S | -0.326 ± 0.006 | -0.323 ± 0.006 | -0.346 ± 0.016 |
| Flatness F | 11.45 ± 0.03 | 11.38 ± 0.03 | 20.39 ± 0.20 |
| η | 0.0244 ± 0.0002 | 0.0244 ± 0.0002 | 0.0241 ± 0.0003 |
| λ | 0.3201 ± 0.0014 | 0.3196 ± 0.0015 | 0.3197 ± 0.0048 |
| L_f | 1.26 ± 0.01 | 1.26 ± 0.01 | 1.25 ± 0.02 |
| τ_k | $(6.30 \pm 0.08)e-3$ | $(6.30 \pm 0.09)e-3$ | $(6.14 \pm 0.15)e-3$ |
| T_e | 0.07235 ± 0.0006 | 0.07213 ± 0.0006 | 0.07220 ± 0.0021 |
| $\Delta T_{ave} / T_e$ | 96.8 | 97.0 | 18.0 |
| $\epsilon L_f / (u')^3$ | 1.335 ± 0.083 | 1.343 ± 0.096 | 1.301 ± 0.145 |

3.2. Forced particle-laden turbulence

We shall now consider forced turbulence laden with solid particles. The same flow parameters adopted for the single phase forced turbulence are used. A particle-laden system involves 4 additional governing parameters: the particle diameter relative to the flow Kolmogorov length of single-phase turbulence d_p/η , particle-to-fluid density ratio ρ_p/ρ_f , particle volume fraction ϕ_v , and particle terminal velocity relative to the Kolmogorov velocity W/v_k . In this preliminary study, we consider non-sedimenting particles ($W = 0$) with a density ratio of $\rho_p/\rho_f = 5$. The particle diameter is set to 8 lattice units when 256^3 grid resolution is used, leading to $d_p/\eta = 8.05$. The volume fraction is fixed at 0.102. This amounts to 6400 solid particles at 256^3 grid resolution.

For this single combination of system parameters, three LB simulations are conducted (Table 2). The purpose here is to examine whether variations of grid resolution and velocity scale affect the physical results.

We shall focus mainly on the statistics at a stationary stage. To gain insights into the dynamics of the particle-laden system, we will report on three levels of analysis. At the first level, we view the particle–fluid system as a continuous system in local velocity, with velocity inside each particle set to that of solid body rotation. The velocity gradients are certainly not continuous at the particle–fluid interface. At the second level, we partition the flow into two parts, the region belong to the fluid and the region within the particles; statistics are computed in each region separately. At the third level, statistics are gathered as a function of distance from the surface of a particle, to elucidate the role of no-slip particle–fluid interfaces.

3.2.1. Level 1: whole field statistics

Table 2 provides the whole field statistics. Evidently, the three particle-laden LB runs generate essentially the same statistics, except the velocity derivative flatness. We suspect that the value of velocity derivative flatness is mostly governed

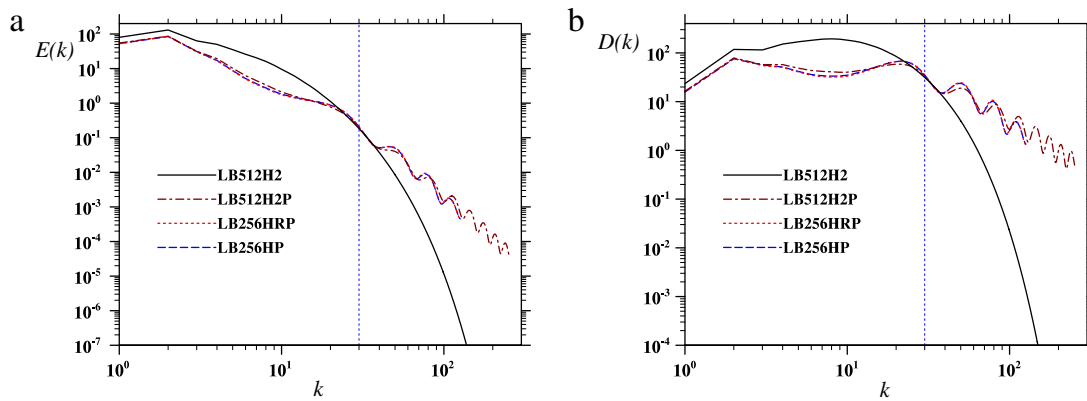


Fig. 6. (a) Kinetic energy and (b) dissipation rate spectra for particle-laden flows. Also shown are the spectra for the single-phase turbulence LB512H2. The vertical line label $k = 30$.

by the large values at the particle–fluid interface. The increased resolution in run LB512H2P provides a better representation of the extreme values leading to a higher value of velocity derivative flatness.

Compared to the single phase turbulence, the magnitude of field-averaged dissipation rate in the particle-laden flow is significantly smaller. Take, for example, the run LB256HRP, the average dissipation rate is 2424, which is 67.7% the value of the corresponding single phase run LB256HR. Since the dissipation rate is still balanced by the large-scale energy input, this implies that the large-scale energy input is also reduced to 67.7% when compared to the single-phase turbulence. This reduction can be roughly explained as follows. First, for the single phase turbulence, we may approximate the forcing energy input as

$$\text{forcing energy rate (SP)} \approx \frac{4N_f \sigma_f^2 T_f}{1 + 1.356 T_f / T_e^{\text{SP}}}, \quad (9)$$

where T_e^{SP} is the eddy turnover time in single-phase turbulence; the coefficient 1.356 is introduced to reproduce the value shown in Table 1 for run LB256HR. For the particle-laden flow, two aspects will reduce the forcing energy input: the forcing is only applied to the region occupied by the fluid, and the field eddy turnover time is reduced. A simple model for the forcing energy input in the particle-laden (PL) flow is

$$\text{forcing energy rate (PL)} \approx (1 - \theta_v) \times \frac{4N_f \sigma_f^2 T_f}{1 + 1.356 T_f / T_e^{\text{PL}}}, \quad (10)$$

where T_e^{PL} is the eddy turnover time in particle-laden turbulence. Using $\theta_v = 0.102$ and $T_e^{\text{PL}} = 0.07213$ from Table 2, we obtain an estimate for forcing energy input at 2849. This is comparable to the value (2424) actually realized, although it does not fully explain the reduction. The simple model assumes that the dissipation rate in the fluid region is uniformly distributed, which is certainly not true—a point we shall return to in Section 3.2.3.

The whole field kinetic energy, $1.5(u')^2$, in the particle-laden flow is about 50% of the single-phase value. In forced particle-laden flow simulation using the point-particle approach, Abdelsamie and Lee [50] found that the system kinetic energy is reduced to 65% of single-phase turbulence for the density ratio of 800 and volume fraction of 5×10^{-4} , and the dissipation rate is reduced to 35%–75% depending on the particle Stokes number. Although the parameter ranges are different, our results are qualitatively similar. The magnitude of the velocity derivative skewness is also reduced. The most interesting quantity is the normalized flow dissipation rate $\epsilon L_f / (u')^3$. It is around 1.34, much larger than the single-phase value of 0.575. This implies that the particle-laden system is much more dissipative than the single-phase turbulence. Physically, the enhanced system dissipation is due to the enhanced local dissipation at the particle–fluid interfaces.

Fig. 6 shows the kinetic energy spectra and the dissipation rate spectra for particle-laden turbulent flows. Also shown for comparison are the respective spectra for single phase forced turbulence run LB512H2. The three particle-laden LB simulations produce essentially the same energy spectrum. The nearly periodic oscillations reflect the discontinuities at the solid–fluid interfaces, qualitatively labeled as the boxcar effect by Lucci et al. [42]. However, these oscillations do not affect the interpretation of the whole-field velocity field, as the realized kinetic energy has the proper interpretation of the average kinetic energy of the whole system containing the fluid phase and solid particles. The energy is attenuated at low wavenumbers including the two forced shells ($0.5 < k < 1.5$ and $1.5 < k < 2.5$) where the large-scale forcing is applied, and is augmented at large wavenumbers. Essentially, the disturbance flows around the solid particles enhance the high-wavenumber energy content, at the cost of reduced low-wavenumber velocity fluctuations. Alternatively, the presence of solid particles increases the resistance to large-scale flow due to the added drag on the solid particles. The pivot wavenumber dividing the two regions is around $k_{\text{pivot}} = 30$ or $k_{\text{pivot}} d_p / (2\pi) = 0.94$. This pivot wavenumber is very similar to what was observed in [43] for decaying turbulence ($k_{\text{pivot}} d_p / (2\pi) \approx 0.9$) at similar particle size, density ratio, and volume fraction. Specifically, $E(k = 1)$ and $E(k = 2)$ in the forced particle-laden turbulence are 69% and 66% of the respective values of

Table 3

Statistics in forced particle-laden turbulence partitioned into the fluid phase and the solid particles. The values from the lattice Boltzmann simulations have been converted to the units in the pseudo-spectral simulation.

| Run | LB256HP | LB256HRP | LB512H2P |
|--|------------------|------------------|------------------|
| d_p/dx | 8 | 8 | 16 |
| N_p | 6400 | 6400 | 6400 |
| ρ_p/ρ_f | 5 | 5 | 5 |
| ϕ_v | 0.102 | 0.102 | 0.102 |
| ϕ_m | 0.510 | 0.510 | 0.510 |
| d_p/η^a | 8.05 | 8.05 | 8.15 |
| d_p/λ^a | 0.614 | 0.614 | 0.614 |
| $St \equiv \frac{1}{18} \frac{\rho_p}{\rho_f} \left(\frac{d_p}{\eta}\right)^2$ | 18.0 | 18.0 | 18.5 |
| ϵ_s^{full} per unit mass | 2414 ± 63 | 2424 ± 73 | 2532 ± 123 |
| $\epsilon^{particle}$ | 0 | 0 | 0 |
| ϵ_s^{fluid} | 2688 ± 70 | 2699 ± 81 | 2820 ± 137 |
| ϵ_p^{fluidb} | 3228 ± 338 | 2820 ± 429 | 2992 ± 348 |
| $\frac{1}{2} \langle \mathbf{u}^2 \rangle_s^{full}$ | 260.6 ± 5.3 | 260.6 ± 6.2 | 272.2 ± 7.8 |
| $\frac{1}{2} \langle \mathbf{u}^2 \rangle_p^{fluid}$ | 267.7 ± 5.4 | 267.8 ± 6.3 | 280.6 ± 8.1 |
| $\frac{1}{2} \langle \mathbf{V}_p^2 \rangle_p$ | 198.2 ± 4.2 | 196.9 ± 5.0 | 197.5 ± 5.5 |
| $\langle \Omega_p^2 \rangle_p$ | 633.4 ± 11.4 | 642.2 ± 12.6 | 627.0 ± 20.6 |
| $\frac{1}{2} \langle \mathbf{V}_p^2 \rangle_p + \frac{1}{20} d_p^2 \langle \Omega_p^2 \rangle_p$ | 199.5 ± 5.5 | 198.2 ± 6.4 | 197.8 ± 8.1 |
| $\frac{1}{4} \langle \omega^2 \rangle_p^{fluid}$ | 6915 ± 181 | 6967 ± 211 | 7262 ± 352 |
| $\nu \langle \omega^2 \rangle_p^{fluid}$ | 2614 ± 69 | 2634 ± 80 | 2745 ± 133 |
| $Re_{p1} \equiv \sqrt{3}(\mathbf{u}' - V_p')d_p/\nu$ | 6.1 | 6.1 | 7.1 |
| $Re_{p2} \equiv \sqrt{\langle \Omega_p^2 \rangle_p} d_p^2/\nu$ | 10.3 | 10.3 | 10.2 |

^a Here η is defined based on the full-field; see Table 2.

^b These values are obtained from one time instant (from the fields saved at the end of simulation, the same used for visualizations).

single-phase turbulence. Part of this reduction is due to the fact that the forcing field is only applied to the fluid lattice node ($1 - \theta_v = 89.8\%$ of space). Another reason could be direct transfer of energy at the solid–fluid interface at the time of forcing application. In contrast, in the decaying particle-laden flows, the energy levels in the forced shells are almost unaffected (see Fig. 33 in Lucci et al. [42], and Fig. 10 in Gao et al. [43]). Interestingly, this distinction in the energy levels in the forced shells between forced and decaying particle-laden flows is also observed in point-particle based simulations (see Fig. 8 in Abdelsamie and Lee [50]). In particular, Abdelsamie and Lee [50] pointed out a direct energy transfer from the forced scales to the small scales, perhaps this is the reason for reduced kinetic energy levels in the forced shells.

3.2.2. Level 2: partitioned statistics

Next, we shall compute statistics within the fluid phase and the solid particles separately. The results are displayed in Table 3. Since, by definition, the local dissipation rate is zero everywhere inside a solid particle, one can infer that the local average dissipation rate within the fluid phase is

$$\epsilon^{fluid} = \frac{1}{1 - \phi_v} \epsilon^{full}, \tag{11}$$

where the superscripts *fluid* and *full* indicate an average over the fluid phase and the full field, respectively. For some quantities, we also have two options of computing the statistics in spectral space and physical space, and they are denoted respectively by subscripts *s* and *p*, respectively, in Table 3.

It can be shown that, with regard to the kinetic energy per unit mass, we have [43]

$$\left\langle \frac{\mathbf{u}^2}{2} \right\rangle^{full} = (1 - \phi_v) \left\langle \frac{\mathbf{u}^2}{2} \right\rangle^{fluid} + \phi_v \left(\frac{1}{2} \langle V_p^2 \rangle + \frac{1}{20} d^2 \langle \Omega_p^2 \rangle \right). \tag{12}$$

The data in Table 3 can be used to confirm that

$$\left\langle \frac{\mathbf{u}^2}{2} \right\rangle_s^{full} = (1 - \phi_v) \left\langle \frac{\mathbf{u}^2}{2} \right\rangle_s^{fluid} + \phi_v \left(\frac{1}{2} \langle V_p^2 \rangle_p + \frac{1}{20} d^2 \langle \Omega_p^2 \rangle_p \right), \tag{13}$$

which demonstrates the precise interpretation of the whole-field statistics discussed in Section 3.2.1.

It is also interesting to examine the average kinetic energy per unit volume for the whole system and we expect

$$\left\langle \rho \frac{\mathbf{u}^2}{2} \right\rangle^{full} = (1 - \phi_v) \rho_f \left\langle \frac{\mathbf{u}^2}{2} \right\rangle^{fluid} + \phi_v \rho_p \left(\frac{1}{2} \langle V_p^2 \rangle + \frac{1}{20} d^2 \langle \Omega_p^2 \rangle \right). \quad (14)$$

Taking, for example, Run LB256HP, with $\rho_f = 1$ and $\rho_p = 5$, we obtain

$$\left\langle \rho \frac{\mathbf{u}^2}{2} \right\rangle^{full} = 267.7 \times (1 - 0.102) + 0.102 \times 5 \times (198.2 + 0.19635^2 \times 633.4/20) = 342.1. \quad (15)$$

This may be compared with the value of the kinetic energy per unit volume of a single phase flow (Run LB256H), 524.5. Namely, the kinetic energy per unit volume of the particle-laden flow is 65% of the value for the single-phase turbulence.

We also observe from Table 3 that, within statistical uncertainty, the following relation is valid:

$$\epsilon^{fluid} \approx \nu \langle \omega^2 \rangle^{fluid}. \quad (16)$$

Namely, the relation for single-phase turbulence remains valid when applied to the particle-laden turbulence within the fluid phase.

In the limit of passive and small particles, it is expected that $\langle \mathbf{V}_p^2 \rangle / \langle \mathbf{u}^2 \rangle^{fluid} = 1$ and $4 \langle \Omega_p^2 \rangle / \langle \omega^2 \rangle^{fluid} = 1$. We have a ratio of $\langle \mathbf{V}_p^2 \rangle / \langle \mathbf{u}^2 \rangle^{fluid} = 0.74, 0.74, 0.70$ and $4 \langle \Omega_p^2 \rangle / \langle \omega^2 \rangle^{fluid} = 0.0916, 0.0921, 0.0863$, respectively, for Runs LB256HP, LB256HRP, and LB5 12H2P. In terms of rms fluctuations, $\langle u' \rangle^{fluid} / V_p' = 0.86, 0.86, 0.84$ and $2 \Omega_p' / \omega' = 0.303, 0.304, 0.294$, respectively, for Runs LB256HP, LB256HRP, and LB5 12H2P. This reduction in particle translational velocity and angular velocity is due to both the finite size (spatial filtering) and inertial filtering. The reduction in angular velocity is much larger due to significant contribution from the small scales which translates to a strong spatial filtering effect.

Finally, the data in Table 3 allow us to estimate particle Reynolds number. Two methods are used and results are shown in the last two rows. It appears that the particle Reynolds number is ~ 10 in the particle-laden flow simulation.

3.2.3. Level 3: profiles relative to the particle surface

To gain some insight into the variations of various quantities near the particle surface, we associate each fluid lattice point with the nearest particle surface. The distance, $r - r_p$, from the nearest particle surface is then calculated, where r is the distance from a fluid lattice node to the center of the nearest particle and r_p is the particle radius ($r_p = 0.5d_p$). This distance is then divided into bins of a given width of $\delta = 0.05r_p$: namely, the i -th bin gathers all fluid lattice points whose distance from the nearest particle surface falls within the range from $(i - 1)\delta$ to $i\delta$.

The average particle center-to-center distance l_p can be estimated as

$$\frac{l_p}{r_p} = \left(\frac{4\pi}{3\phi_v} \right)^{1/3} \approx 3.45. \quad (17)$$

For small $(r - r_p)/r_p$, the number of fluid lattice points in i -th bin, $n_b(i)$, may be estimated as

$$\frac{n_b(i)}{N^3} = \frac{4}{3}\pi [(r_p + i\delta)^3 - (r_p + i\delta - \delta)^3] \frac{N_p}{N^3} = \{ [1 + 0.05i]^3 - [1 + 0.05(i - 1)]^3 \} \phi_v. \quad (18)$$

If the solid particles are placed in a regular array, the above formula will apply till $r/r_p = 0.5l_p/r_p = 1.725$ and $n_b(i)$ would reach a maximum at $r/R = 1.725$.

Fig. 7 shows $n_b(i)$ as a function of r , in both linear–log and linear–linear plot, calculated from one time instant at the end of the simulations; Eq. (18) gives a reasonable prediction when $r/r_p < 1.4$. The location of maximum $n_b(i)$ appears to occur indeed at $r/r_p \approx 1.725$; however, the maximum value is significantly less than the prediction by Eq. (18) due to irregular solid particle distribution. The maximum distance was found to be around $r/r_p = 6.0$, significantly larger than $0.5\sqrt{2}l_p/R = 2.44$ for a perfectly regular arrangement of solid particles. This implies that solid particles exhibit some level of preferential concentration. However, the value to $n_b(i)$ is negligibly small when $r/r_p > 4.0$. It should be noted that $n_b(i)$ in Fig. 7 is computed based on a single time for each simulation, so the values of $n_b(i)$ at large r/d_p are subject to significant statistical uncertainties.

Fig. 8(a) is a snapshot of fluid vorticity distribution on a slice at $z = 128.5$ from Run LB256HRP. It is clear that there are patches of high vorticity near the surfaces of solid particles due to the viscous boundary layers. Occasionally, there is even evidence of vortex shedding (see, for example, the wake associated with a particle in the lower left portion of the slice). It could be possible that the turbulent background field might induce vortex-shedding at much lower particle Reynolds number (also keep in mind that the local particle Reynolds number could be significantly higher than the estimated average value of ~ 10). In Fig. 8(b) we plot the bin-averaged normalized enstrophy as a function of r , revealing several interesting features. First, the bin-averaged enstrophy is larger than the mean for $(r - r_p) < 0.4r_p$ and less than the mean for $(r - r_p) > 0.4r_p$. There is a peak normalized enstrophy very close to the particle surface, with a peak value of ~ 4.3 to 7 depending on the grid resolution. The peak occurs at $(r - r_p)/r_p = 1.175$ for the two 256^3 runs and at $(r - r_p)/r_p = 1.075$

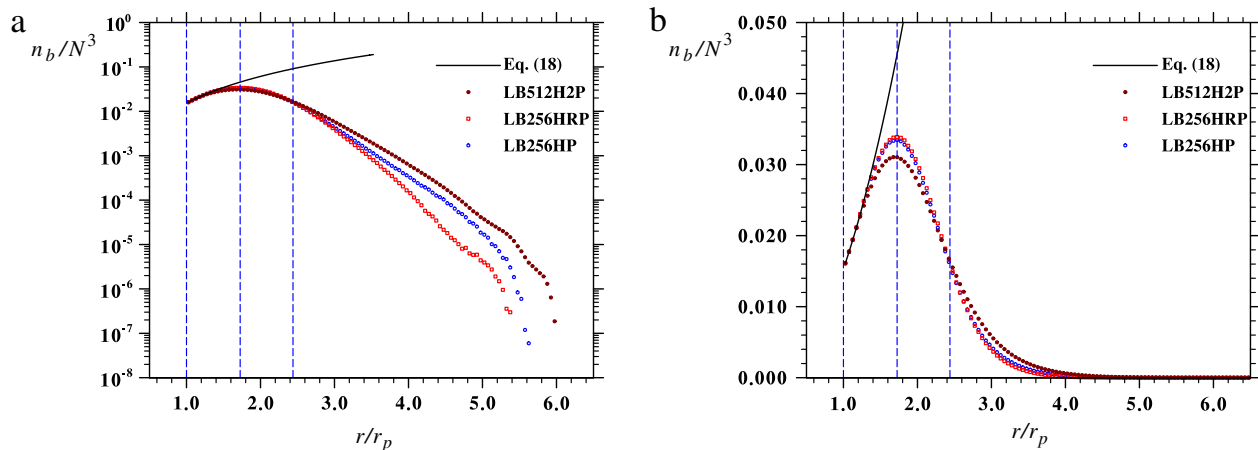


Fig. 7. The number of fluid lattice points in a given bin as a function of distance from the particle center: (a) linear–log plot; (b) linear–linear plot. The three vertical lines mark the locations of $r/r_p = 1, 1.725,$ and $2.44,$ respectively.

for the LB512H2P. This implies that the vorticity is not fully resolved at 256^3 , causing some numerical diffusion near the particle surface. Interestingly, there is also a weak minimum of $\omega^2/\langle\omega^2\rangle^{fluid} = 0.44$ at $(r - r_p)/r_p \approx 1.0$, regardless of the resolutions. The bin-averaged enstrophy seems to increase with distance slowly after the minimum. Finally, Fig. 8(c) shows the relative contribution from each bin to the total fluid enstrophy; namely, the weighted bin value is defined as

$$\frac{[\omega(i)]^2 n_b(i)}{\sum [\omega(i)]^2 n_b(i)} \frac{1}{\delta/r_p}, \tag{19}$$

so that the area under each curve in Fig. 8(c) is exactly one. A reasonable estimate of the boundary layer thickness is $0.4r_p$ —the location where the normalized vorticity crosses 1.0. We found that this 19.5% of the spatial region with $(r - r_p) < 0.4r_p$ contributes to about 57.5% of the total fluid enstrophy regardless of the grid resolution, revealing the dominant role of the viscous boundary layer at the solid particle surface in the enstrophy budget.

A similar analysis is performed for the local dissipation rate (Fig. 9). Visualization of strain-rate magnitude (Fig. 9(a)) shows that patches of high strain rate tend to be found near the particle surfaces. Regions of high strain rate are typically nearby regions of high vorticity, but appear to be less structured when compared to the vorticity distribution. The bin-averaged normalized local-dissipation value decreases monotonically with r (Fig. 9(b)), with values larger than the mean for $(r - r_p)/r_p < 0.4$ and smaller than the mean otherwise. The maximum value near the surface could reach 5.6–8.0, and again depends on grid resolution. The value away far from the surface is around 0.38. The relative contributions (Fig. 9(c)) from various bins drop rapidly with r , especially near the particle surface. The 19.5% of the spatial region with $(r - r_p) < 0.4r_p$ contributes to around 52.3% of the total viscous dissipation, comparable to but slightly less than the enstrophy concentration in this region.

We also analyze this bin dependence for local velocity magnitude and kinetic energy (Fig. 10). The visualization on the same slice shows, in contrast to vorticity and strain rate, that the fluid velocity magnitude is less near the particle surface, as expected from the no-slip condition and the lower particle velocity fluctuations ($u'/V'_p \approx 0.85$; see Table 3). This is clearly demonstrated in Fig. 10(b) when the bin averaged kinetic energy is quantified. Indeed, the local kinetic energy matches that of the solid particles at the particle surface, and increases with r for $r/r_p < 3$. The trend for $r/r_p > 3$ is not clear and also subject to large statistical uncertainties. The relative contribution (Fig. 10(c)) shows a peak at $r/r_p = 1.775$. The 19.5% of the spatial region with $(r - r_p) < 0.4r_p$ contributes to only $\sim 16.1\%$ of the total kinetic energy. If the separation is too large, there is no sample (see Fig. 7(a)), then a zero value is assigned.

Taken together, the above analyses demonstrate that the region $((r - r_p) < 0.4r_p)$ near the particle surface exhibits high strain rate and high vorticity, but low kinetic energy, due to the presence of solid particles of higher inertia. It is hoped that the profiles presented here could provide a starting point for parameterizing the turbulence statistics in particle-laden flow.

3.3. Transient evolution for Run LB512H2P

In this section, we show transient evolution for Run LB512H2P. Initially we ran the single-phase flow simulation (Run LB512H2) to a stationary stage. Solid particles were then introduced at $t = 1.6$ with velocity of a given particle set to the local fluid velocity at the center of the particle and angular velocity set to zero.

Fig. 11 displays the time evolution of whole-field kinetic energy and dissipation rate for both Run LB512H2P and Run LB512H2. The kinetic energy of the system drops quickly immediately after the introduction of solid particles and then settles to the stationary stage with mean values consistent with those obtained from 256^3 runs. In contrast, the dissipation rate jumps by a factor of 2 immediately after the release of particles, due to the discontinuity of velocity at the solid–fluid interfaces, very similar to the results reported for decaying particle-laden flows [43]. The transition to the stationary stage for

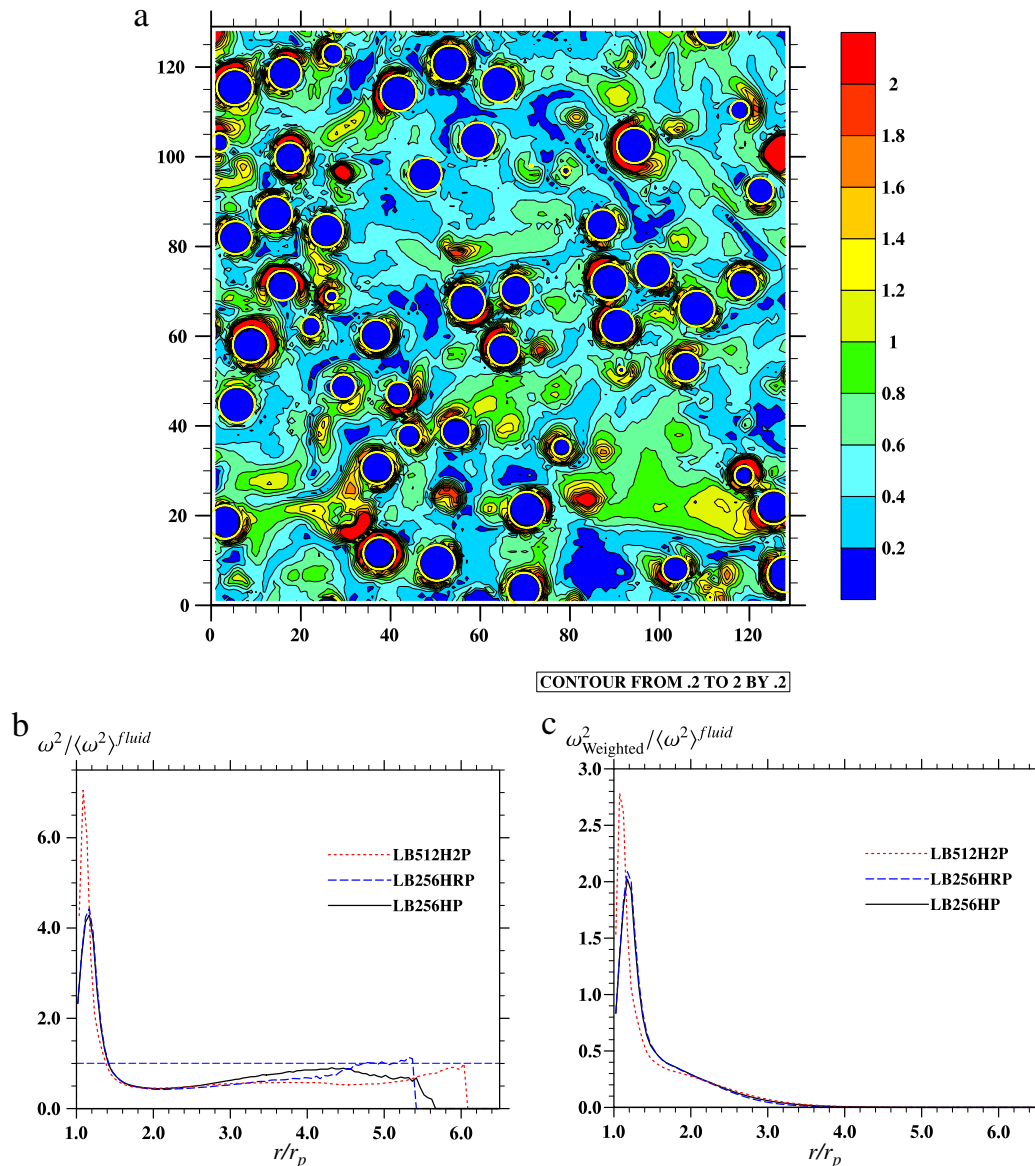


Fig. 8. (a) Contours of fluid vorticity magnitude $|\omega|/\sqrt{\langle\omega^2\rangle^{fluid}}$ and particle position in an x - y plane at $z = 128.5$, at the end of simulation from LB256HRP. Only a quarter of the plane is shown. (b) Profile of bin-averaged $\omega^2/\langle\omega^2\rangle^{fluid}$ as a function of distance from the center of a solid particle. The horizontal line marks the level 1.0. (c) Weighted bin-averaged $\omega^2/\langle\omega^2\rangle^{fluid}$ as a function of distance from the center of a solid particle.

both kinetic energy and dissipation rate contains two phases: a fast relaxation phase taking about one to two eddy turnover times, followed by a slow relaxation phase lasting about 4–5 eddy turnover times. The stationary-stage average dissipation is consistent with those from 256^3 runs.

The evolutions of velocity-derivative skewness and flatness are shown in Fig. 12. The magnitudes of stationary-stage skewness are slightly larger than those from 256^3 runs. The stationary-stage flatness for Run LB512H2P is much larger than the corresponding 256^3 runs, as previously noted, due to the better resolution of velocity gradient near the particle surfaces which seems to dominate the overall magnitude of velocity-derivative flatness. As indicated previously, this local grid-dependence, however, does not affect the overall coupling between the fluid phase and solid particles. The flatness value for particle-laden flows are significantly larger than that of single-phase turbulence.

4. Summary and outlook

In this study, we have applied the mesoscopic lattice Boltzmann (LB) method to simulations of both single-phase turbulence and particle-laden turbulence which are maintained by large-scale forcing. Forced stationary flows allow averaging to be taken over time, to obtain better average statistics. The disturbance flows around finite-size solid particles are resolved, providing the opportunity to study the detailed interactions between fluid turbulence and solid particles at the particle–fluid interfaces. This particle-resolved simulation (PRS) approach is much more general than the previous point-particle simula-

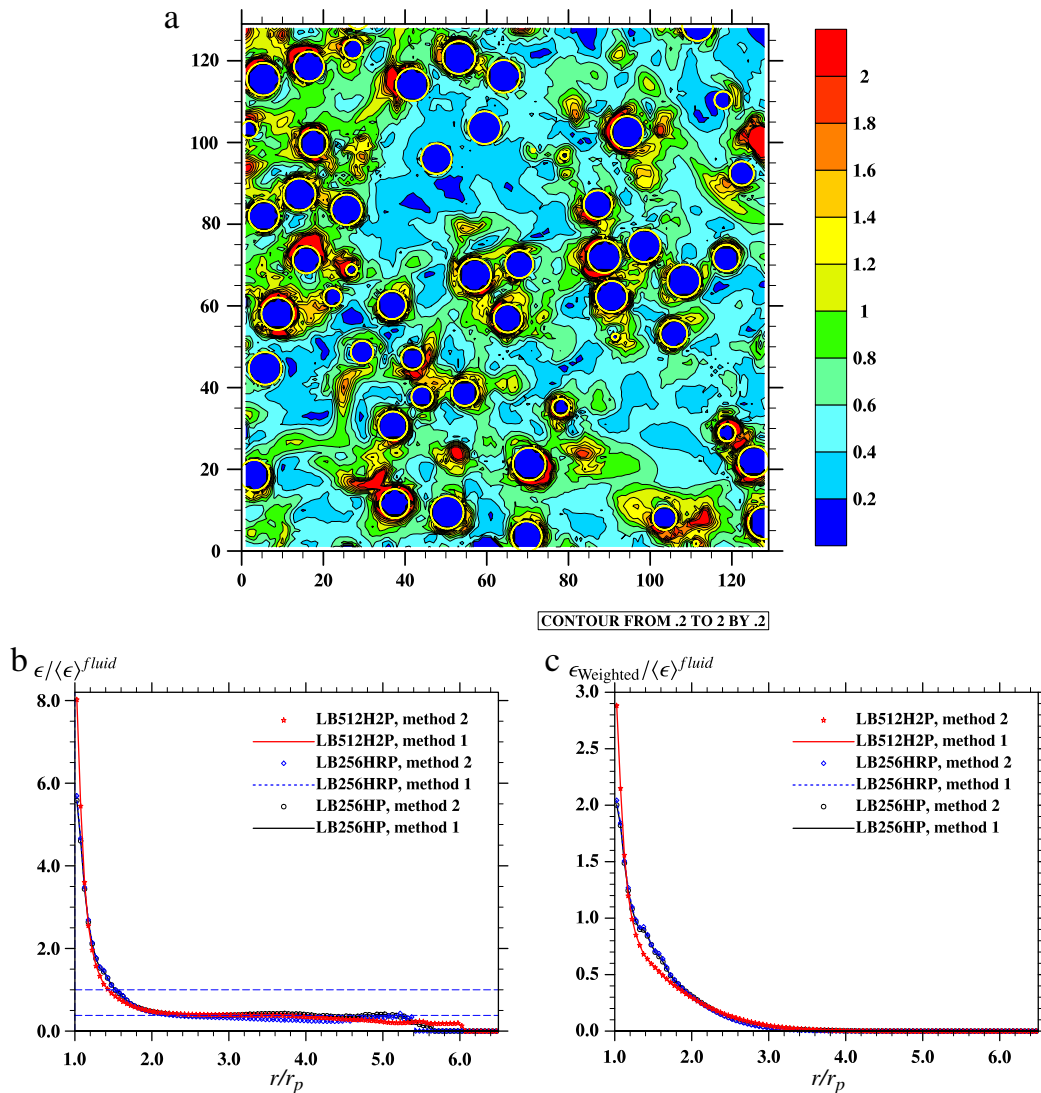


Fig. 9. (a) Contour of normalized local strain rate $\sqrt{\epsilon / \langle \epsilon \rangle^{fluid}}$ and particle position in an $x-y$ plane at $z = 128.5$, at the end of simulation from LB256HRP. Only a quarter of the plane is shown. (b) The profile of bin-averaged $\epsilon / \langle \epsilon \rangle^{fluid}$ as a function of distance from the center of a solid particle. The two horizontal lines mark the levels of 1.0 and 0.38, respectively. (c) Weighted bin-averaged $\epsilon / \langle \epsilon \rangle^{fluid}$ as a function of distance from the center of a solid particle.

tion (PPS) approach [3], and is expected to become a quantitative research tool for particle-laden turbulent flows as better computational resources are becoming available. This study may be viewed as a continuation of two recent studies, one on the comparison of pseudo-spectral and LB simulations of single-phase decaying turbulence [54] and the other on the simulation of decaying particle-laden turbulence [43].

We have demonstrated that the popular nonuniform time-dependent stochastic forcing scheme of Eswaran and Pope [49] can be implemented in the mesoscopic MRT LB approach following the formulation of Lu et al. [53]. The statistics of single-phase forced turbulence obtained from the MRT LB approach are in excellent agreement with those from the pseudo-spectral simulations, provided that the grid resolution in the LB simulation is doubled. We also demonstrated that the flow statistics is not sensitive to the velocity scale used for the LB simulation, even when the local maximum velocity is as large as 0.25 in lattice units. We did, however, observe larger fluctuations in the velocity derivative skewness when compared to the pseudo-spectral results, resulting from acoustic waves in the system as noted in [54]. We conclude that the MRT LB method is a reliable and accurate method for direct numerical simulation of forced homogeneous isotropic turbulence.

Preliminary results on forced turbulence laden with non-sedimenting solid particles at $\rho_p / \rho_f = 5$, $\phi_v = 0.102$, and $d_p / \eta = 8.05$ have been presented. While only one specific parameter setting is considered, a systematic analysis of the particle-laden flow has been carried out. The analysis is performed at three levels: whole-field, phase-partitioned, and profiles as a function of distance from the surface of solid particles. Several important conclusions have been reached. First, we have shown that the particle-laden turbulence is much more dissipative in terms of the non-dimensional dissipation rate ($\epsilon^{full}_{L_f} / (u')^3 = 1.34$), when compared to the single-phase forced turbulence ($\epsilon^{full}_{L_f} / (u')^3 = 0.575$). Part of this difference is related to the difference in the effective flow Reynolds number (see Fig. 2 in Ishihara et al. [58]), which is $R_\lambda = 45$ for the particle-laden flow and $R_\lambda = 74$ for the single-phase turbulence. If we take the data from Fig. 2 in Ishihara et al. [58], the value of $\epsilon^{full}_{L_f} / (u')^3$ for single-phase turbulence at $R_\lambda = 45$ would be in the range of 0.7–1.0, still significantly less than

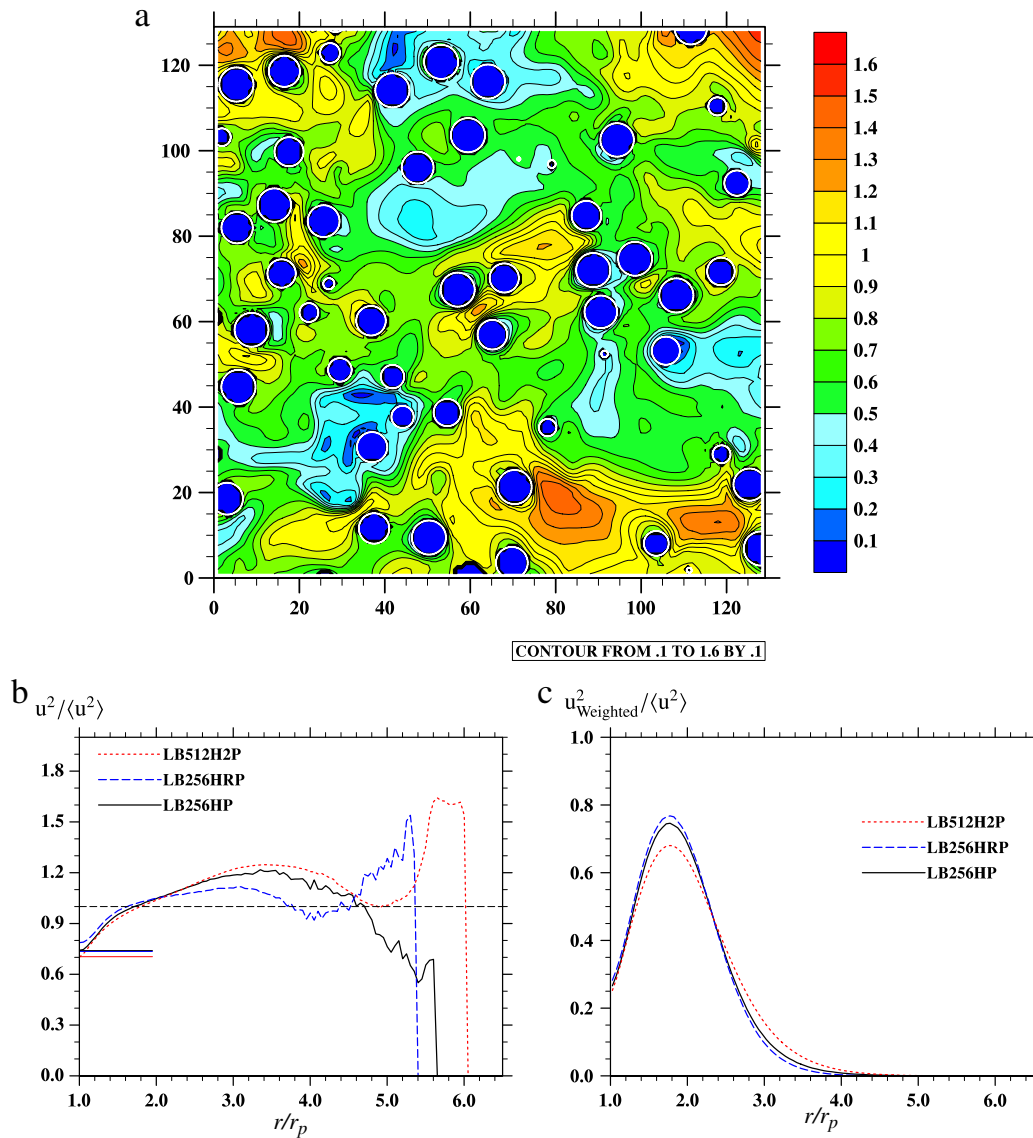


Fig. 10. (a) Contour of normalized local velocity fluctuation $\sqrt{\mathbf{u}^2 / \langle \mathbf{u}^2 \rangle}$ and particle position in an x - y plane at $z = 128.5$, at the end of simulation from LB256HRP. Only a quarter of the plane is shown. (b) The profile of bin-averaged $u^2 / \langle u^2 \rangle$ as a function of distance from the center of a solid particle. The long horizontal line marks the level of 1.0, and the three short horizontal lines mark 0.740, 0.735, and 0.704, the respective solid-particle rms velocity for the runs. (c) Weighted bin-averaged $u^2 / \langle u^2 \rangle$ as a function of distance from the center of a solid particle.

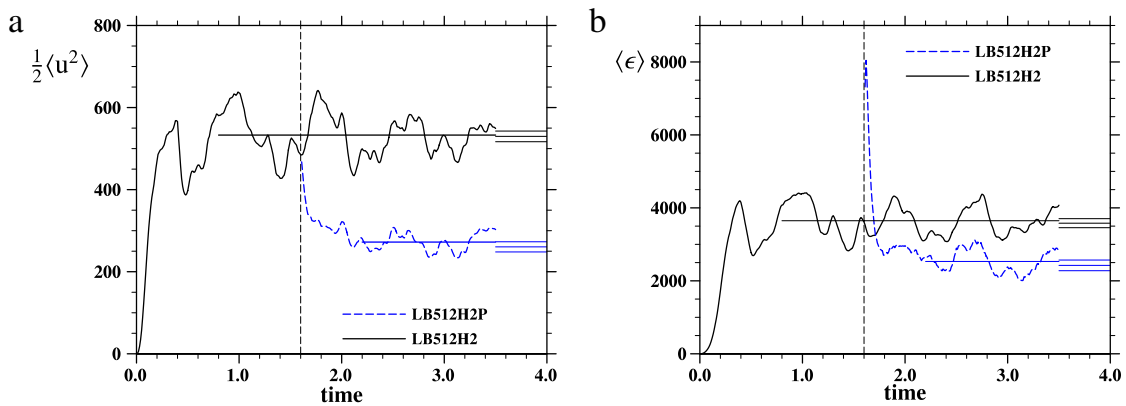


Fig. 11. Evolution of (a) kinetic energy and (b) dissipation rate after particles are introduced, relative to the single-phase turbulence. The vertical dash line shows the time when the particles are introduced. The mean values are marked by horizontal lines through the data, with the lines spanning the time intervals used for computing them. The short horizontal lines on the very right show the mean and two standard deviations from LB256HR and LB256HRP.

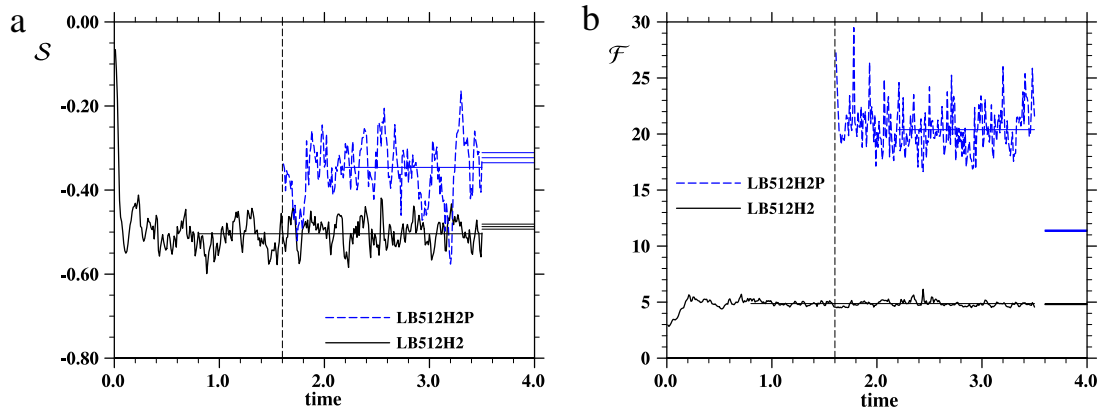


Fig. 12. Evolution of (a) velocity-derivative skewness \mathcal{S} and (b) flatness \mathcal{F} , relative to the single-phase turbulence. The mean values are marked by horizontal lines through the data, with the lines spanning the time intervals for computing them. The short horizontal lines on the very right show the mean and two standard deviations from LB256HR and LB256HRP.

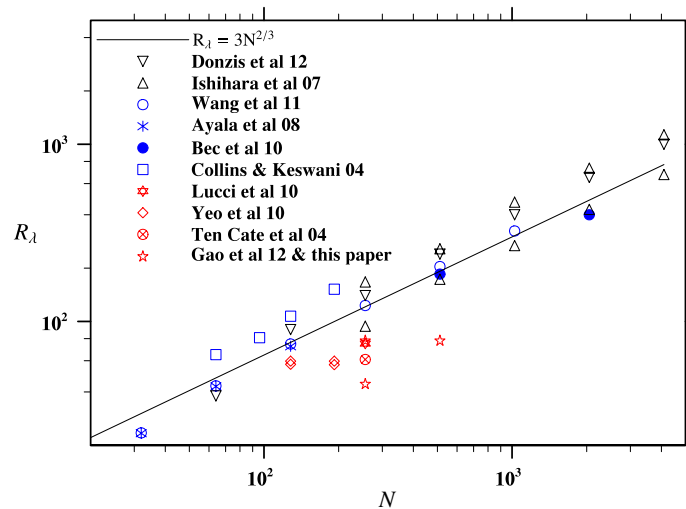


Fig. 13. Simulated flow Taylor-microscale Reynolds number, R_λ , as a function of grid resolution, for published single-phase turbulence simulations (black symbols), point-particle simulations (blue symbols) and particle-resolved simulations (red symbols) of turbulent particle-laden flows. The line denotes the fitted theoretical scaling for single-phase turbulence DNS. (For interpretation of the references to colour in this figure legend, the reader is referred to the web version of this article.)

1.34 in our particle-laden turbulence. The reason for the higher dissipative nature of the particle-laden turbulence has been shown to be related to the higher dissipation near the particle surface as a viscous boundary layer is present due to the difference in the velocity fluctuations between the fluid phase and the solid particles. The thickness of the boundary layer is estimated to be about $0.4r_p$. While this near-surface region accounts for 19.5% of the space within the fluid, it contributes to 57.5% of total viscous dissipation. We also found that the vorticity magnitude exhibits a maximum inside the boundary layer and a minimum outside the boundary layer, showing detachment of the vorticity structure from the solid surface. The sharp gradients near the particle surface contribute dominantly to the value of velocity derivative flatness, making the flatness in particle-laden flow much larger than that of single-phase turbulence.

In the spectral space, the presence of solid particles attenuates energy at large scales including the forcing shells and augments energy at the small scales. This differs from the results for decaying particle-laden turbulence in that there the energy in the lowest shells are not altered by particles. This distinction between forced and decaying particle-laden flows has been shown previously in [50] using PPS. On the other hand, the pivot wavenumber is found to be very similar to the value found in decaying particle-laden turbulence under the similar parameter setting [43].

Due to the limited space, we have not analyzed fully the statistics of the particle-laden turbulence. For example, it would be interesting to examine the probability density functions of local velocity, local velocity-gradient, local dissipation rate, and local vorticity, and compare them with those of single-phase flows. The distribution and collision rate of solid particles may also be studied [31].

We must emphasize the preliminary nature of the results presented in this paper. In general, PRS is still in its very early stage, and results are limited in the range of resolved length and time scales covered. The range of explicitly resolved scales is crucial in any numerical simulation of turbulent single-phase and multiphase flows. Fig. 13 summarizes the resolutions that have been achieved in direct numerical simulations (DNS) of single-phase turbulence, PPS, and PRS. Due to the increased

complexities of multiphase flows, the resolutions of both PPS and PRS are behind those of the single-phase turbulence DNS. Tracking the interactions of a large-number of particles in a turbulent flow is computationally more intensive than the simulation of carrier fluid turbulence [10]. In PPS, the resolution is determined by the need to resolve the Kolmogorov scale η . This requires a grid spacing of $dx \approx 2\eta$ in a pseudo-spectral simulation or $dx \approx \eta$ in a LB simulation [54,59]. The grid resolution then dictates the ratio of integral scale to Kolmogorov length, L/η . However, PRS using the LB approach requires the grid spacing dx that can simultaneously resolve η , the particle size, and the viscous boundary layer around a particle [27,38]. Namely, $(dx)_{\text{PRS}} = \min(\eta, 0.1d_p, d_p/\sqrt{Re_p})$, where Re_p is the particle Reynolds number based on slip velocity between the phases. Therefore, the resolution requirement in PRS is higher than that in PPS. These explain that, for a given grid resolution, the realized flow R_λ in PRS is lower than that in PPS (Fig. 1).

Clearly, it is desired that PRS sufficiently separates scales in terms of both L_f/η and L/d_p so that the phase interactions and coarse-grained multiphase turbulence characteristics can be meaningfully examined. To this end, highly-scalable PRS codes such as the LB approach used here will need to be applied to broaden the parameter ranges. Our ultimate goal is to bridge PRS and PPS by significantly increasing the range of length scales resolvable in PRS.

Acknowledgments

This work was supported by the US National Science Foundation (NSF) under grants CBET-1235974, OCI-0904534, and CRI-0958512. LPW also acknowledges support from the Ministry of Education of PR China and Huazhong University of Science and Technology through Chang Jiang Scholar Visiting Professorship. Computing resources are provided by National Center for Atmospheric Research through CISL-35751010, CISL-35751014, and CISL-35751015 and by University of Delaware through NSF CRI 0958512.

References

- [1] S. Balachandar, J.K. Eaton, Turbulent dispersed multiphase flow, *Annu. Rev. Fluid Mech.* 42 (2010) 111–133.
- [2] M.R. Maxey, J.J. Riley, Equation of motion for a small rigid sphere in a nonuniform flow, *Phys. Fluids* 26 (1983) 883–889.
- [3] L.-P. Wang, B. Rosa, H. Gao, G.W. He, G.D. Jin, Turbulent collision of inertial particles: point-particle based, hybrid simulations and beyond, *Int. J. Multiph. Flow* 35 (2009) 854–867.
- [4] K.D. Squires, J.K. Eaton, Preferential concentration of particles by turbulence, *Phys. Fluids A* 3 (1991) 1169–1179.
- [5] L.-P. Wang, M.R. Maxey, Settling velocity and concentration distribution of heavy particles in homogeneous isotropic turbulence, *J. Fluid Mech.* 256 (1993) 27–68.
- [6] K.D. Squires, J.K. Eaton, Particle response and turbulence modification in isotropic turbulence, *Phys. Fluids A* 2 (1990) 1191–1203.
- [7] S. Elghobashi, G. Truesdell, On the two-way interaction between homogeneous turbulence and dispersed solid particles. I: turbulence modification, *Phys. Fluids* 5 (1993) 1790–1801.
- [8] S. Sundaram, L.R. Collins, Collision statistics in an isotropic particle-laden turbulent suspension, part 1, direct numerical simulations, *J. Fluid Mech.* 335 (1997) 75–109.
- [9] Y. Zhou, A.S. Wexler, L.-P. Wang, Modelling turbulent collision of bidisperse inertial particles, *J. Fluid Mech.* 433 (2001) 77–104.
- [10] O. Ayala, W.W. Grabowski, L.-P. Wang, A hybrid approach for simulating turbulent collisions of hydrodynamically-interacting particles, *J. Comput. Phys.* 225 (2007) 51–73.
- [11] G.D. Jin, G.-W. He, L.-P. Wang, Large eddy simulation of collisional statistics of inertial particles in isotropic turbulence, *Phys. Fluids* 22 (2010) 055106.
- [12] T.M. Burton, J.K. Eaton, Fully resolved simulations of particle-turbulence interaction, *J. Fluid Mech.* 545 (2005) 67–111.
- [13] H. Hu, Direct simulation of solid–liquid mixtures, *Int. J. Multiph. Flow* 22 (1996) 335–352.
- [14] A.A. Johnson, T.E. Tezduyar, Advanced mesh generation and update methods for 3D flow simulations, *Comput. Mech.* 23 (1999) 130–143.
- [15] H. Hu, N.A. Patankar, M.Y. Zhu, Direct numerical simulations of solid–liquid systems using the arbitrary Lagrangian–Eulerian technique, *J. Comput. Phys.* 169 (2001) 427–462.
- [16] N.A. Patankar, P. Singh, D. Joseph, R. Glowinski, T.W. Pan, A new formulation of the distributed Lagrange multiplier/fictitious domain method for particulate flows, *Int. J. Multiph. Flow* 26 (2000) 1509–1524.
- [17] R. Glowinski, T. Pan, T. Hesla, D. Joseph, J. Périaux, A fictitious domain approach to the direct numerical simulation of incompressible viscous flow passed moving rigid bodies: application to particulate flow, *J. Comput. Phys.* 169 (2001) 363–426.
- [18] T.-H. Wu, X.-M. Shao, Z.-S. Yu, Fully resolved numerical simulation of turbulent pipe flows laden with large neutrally-buoyant particles, *J. Hydrodyn.* 23 (2011) 21–25.
- [19] X. Shao, T. Wu, Z. Yu, Fully resolved numerical simulation of particle-laden turbulent flow in a horizontal channel at a low Reynolds number, *J. Fluid Mech.* 693 (2012) 319–344. <http://dx.doi.org/10.1017/jfm.2011.533>.
- [20] C. Peskin, The immersed boundary method, *Acta Numer.* 11 (2002) 479–517.
- [21] M. Uhlmann, An immersed boundary method with direct forcing for the simulation of particulate flows, *J. Comput. Phys.* 209 (2005) 448–476.
- [22] M. Uhlmann, Interface-resolved direct numerical simulation of vertical particulate channel flow in the turbulent regime, *Phys. Fluids* 20 (2008) 053305.
- [23] M.R. Maxey, B.K. Patel, Localized force representations for particles sedimenting in Stokes flows, *Int. J. Multiph. Flow* 27 (2001) 1603–1626.
- [24] K. Yeo, S. Dong, E. Climent, M.R. Maxey, Modulation of homogeneous turbulence seeded with finite size bubbles or particles, *Int. J. Multiph. Flow* 36 (2010) 221–233.
- [25] S. Takagi, H. Oğuz, Z. Zhang, A. Prosperetti, Physalis: a new method for particle simulation, part II: two-dimensional Navier–Stokes flow around cylinders, *J. Comput. Phys.* 187 (2003) 371–390.
- [26] Z. Zhang, A. Prosperetti, A method for particle simulation, *J. Appl. Mech. Trans. ASME* 70 (2003) 64–74.
- [27] Z. Zhang, A. Prosperetti, A second-order method for three-dimensional particle simulation, *J. Comput. Phys.* 210 (2005) 292–324.
- [28] H. Homann, J. Bec, Finite-size effects in the dynamics of neutrally buoyant particles in turbulent flow, *J. Fluid Mech.* 651 (2010) 81–91.
- [29] C.K. Aidun, Y. Lu, E.J. Ding, Direct analysis of particulate suspensions with inertia using the discrete Boltzmann equation, *J. Fluid Mech.* 373 (1998) 287–311.
- [30] A.J.C. Ladd, Numerical simulations of particulate suspensions via a discretized Boltzmann equation, part 1, theoretical foundation, *J. Fluid Mech.* 271 (1994) 285–309; Part 2. Numerical results, *J. Fluid Mech.* 271 (1994) 311–339.
- [31] A. Ten Cate, J.J. Derksen, L.M. Portela, H.E.A. van den Akker, Fully resolved simulations of colliding monodisperse spheres in forced isotropic turbulence, *J. Fluid Mech.* 519 (2004) 233–271.
- [32] Z.G. Feng, E.E. Michaelides, The immersed boundary–lattice Boltzmann method for solving fluid particles interaction problems, *J. Comput. Phys.* 195 (2004) 602–628.

- [33] Z.G. Feng, E.E. Michaelides, Proteus: a direct forcing method in the simulations of particulate flows, *J. Comput. Phys.* 202 (2005) 20–51.
- [34] N.Q. Nguyen, A.J.C. Ladd, Lubrication corrections for lattice Boltzmann simulations of particle suspensions, *Phys. Rev. E* 66 (2002) 046708.
- [35] D. Qi, Lattice-Boltzmann simulations of particles in non-zero-Reynolds-number flows, *J. Fluid Mech.* 385 (1999) 41–62.
- [36] E.-J. Ding, C.K. Aidun, The dynamics and scaling law for particles suspended in shear flow with inertia, *J. Fluid Mech.* 423 (2000) 317–344.
- [37] E. Climent, M.R. Maxey, Numerical simulations of random suspensions at finite Reynolds numbers, *Int. J. Multiph. Flow* 29 (2003) 579–601.
- [38] A. Naso, A. Prosperetti, The interaction between a solid particle and turbulent flow, *New J. Phys.* 12 (2010) 033040.
- [39] J. Kim, S. Balachandar, Mean and fluctuating components of drag and lift forces on an isolated finite-sized particle in turbulence, *Theor. Comput. Fluid Dyn.* 26 (2012) 1–4.
- [40] Y. Xu, S. Subramaniam, Effect of particle clusters on carrier flow turbulence: a direct numerical simulation study, *Flow Turb. Comb.* 85 (2010) 735–761.
- [41] S. Tenneti, R. Garg, S. Subramaniam, Drag law for monodisperse gas–solid systems using particle-resolved direct numerical simulation of flow past fixed assemblies of spheres, *Int. J. Multiph. Flow* 37 (2011) 1072–1092.
- [42] F. Lucci, A. Ferrante, S. Elghobashi, Modulation of isotropic turbulence by particles of Taylor length-scale size, *J. Fluid Mech.* 650 (2010) 5–55.
- [43] H. Gao, H. Li, L.-P. Wang, Lattice Boltzmann simulation of turbulent flow laden with finite-size particles, *Comput. Math. Appl.* 65 (2013) 194–210. <http://dx.doi.org/10.1016/j.camwa.2011.06.028>.
- [44] D. d’Humières, I. Ginzburg, M. Krafczyk, P. Lallemand, L.-S. Luo, Multiple-relaxation-time lattice Boltzmann models in three-dimensions, *Philos. Trans. R. Soc. Lond. A Math. Phys. Eng. Sci.* 360 (2002) 437–451.
- [45] P. Lallemand, L.-S. Luo, Lattice Boltzmann method for moving boundaries, *J. Comput. Phys.* 184 (2003) 406–421.
- [46] A. Caiazzo, Analysis of lattice Boltzmann nodes initialisation in moving boundary problems, *Prog. Comput. Fluid Dyn.* 8 (2008) 3–10.
- [47] N.Q. Nguyen, A.J.C. Ladd, Lubrication corrections for lattice-Boltzmann simulations of particle suspensions, *Phys. Rev. E* 66 (2002) 046708.
- [48] S.L. Dance, M.R. Maxey, Incorporation of lubrication effects into the force-coupling method for particulate two-phase flow, *J. Comput. Phys.* 189 (2003) 212–238.
- [49] V. Eswaran, S.B. Pope, An examination of forcing in direct numerical simulations of turbulence, *Comput. & Fluids* 6 (1988) 257–278.
- [50] A.H. Abdelsamie, C. Lee, Decaying versus stationary turbulence in particle-laden isotropic turbulence: turbulence modulation mechanism, *Phys. Fluids* 24 (2012) 015106.
- [51] O. Ayala, L.P. Wang, Parallel implementation and scalability analysis of 3D fast Fourier transform using 2D domain decomposition, *Parallel Comput.* 39 (2013) 58–77.
- [52] Z. Guo, C. Zheng, B. Shi, Discrete lattice effects on the forcing term in the lattice Boltzmann method, *Phys. Rev. E* 65 (2002) 046308.
- [53] J. Lu, H. Han, B. Shi, Z. Guo, Immersed boundary lattice Boltzmann model based on multiple relaxation times, *Phys. Rev. E* 85 (2012) 016711.
- [54] Y. Peng, W. Liao, L.-S. Luo, L.-P. Wang, Comparison of the lattice Boltzmann and pseudo-spectral methods for decaying turbulence, part I, low-order statistics, *Comput. Fluids* 39 (2010) 568–591.
- [55] A. Ten Cate, E. Vilet, J. Derksen, H. Van en Akker, Application of spectral forcing in lattice-Boltzmann simulations of homogeneous turbulence, *Comput. & Fluids* 35 (2006) 1239–1251.
- [56] W.A. Kareem, S. Izawa, A.K. Xiong, Y. Fukunishi, Extraction and tracking of multi-scaled vortices from a homogeneous isotropic turbulent field, *J. Turbul.* 8 (N12) (2007) 1–15. <http://dx.doi.org/10.1080/14685240600990274>.
- [57] W. Abdel Kareem, Study of the characteristics of forced homogeneous turbulence using band-pass Fourier filtering, *J. Mech. Sci. Tech.* 26 (2012) 799–809. <http://dx.doi.org/10.1007/s12206-011-1238-6>.
- [58] T. Ishihara, T. Gotoh, Y. Kaneda, Study of high Reynolds number isotropic turbulence by direct numerical simulation, *Annu. Rev. Fluid Mech.* 41 (2009) 165–180.
- [59] P. Moin, K. Mahesh, Direct numerical simulation: a tool in turbulence research, *Annu. Rev. Fluid Mech.* 30 (1998) 539–578.